Measurement of the $B_c^{\pm}$ production cross section in $p\bar{p}$ collisions at $\sqrt{s} = 1.96$ TeV

T. Aaltonen,[21] S. Amerio,[39a,39b] D. Amidei,[31] A. Anastassov,[15,w] A. Annovi,[17] J. Antos,[12] G. Apollinari,[15] J. A. Appel,[15] T. Arisawa,[51] A. Artikov,[13] J. Asaadi,[47] W. Ashmanskas,[15] B. Auerbach,[2] A. Aurisano,[47] F. Azfar,[38] W. Badgett,[15] T. Bae,[25] A. Barbaro-Galtieri,[26] V. E. Barnes,[43] B. A. Barnett,[23] P. Barria,[41a,41c] P. Bartos,[12] M. Bauce,[39a,39b] F. Bedeschi,[41a] S. Behari,[15] G. Bellettini,[41a,41b] J. Bellinger,[53] D. Benjamin,[14] A. Beretvas,[15] A. Bhatti,[45] K. R. Bland,[5] B. Blumenfeld,[23] A. Bocci,[14] A. Bodek,[44] D. Bortoletto,[43] J. Boudreau,[42] A. Boveia,[11] L. Brigliadori,[6a,6b] C. Bromberg,[32] E. Brucken,[21] J. Budagov,[13] H. S. Budd,[44] K. Burkett,[15] G. Busetto,[39a,39b] P. Bussey,[19] P. Butti,[41a,41b] A. Buzatu,[19] A. Calamba,[10] S. Camarda,[4] M. Campanelli,[28] F. Canelli,[11,ee] B. Carls,[22] D. Carlsmith,[53] R. Carosi,[41a] S. Carrillo,[16,l] B. Casal,[9,j] M. Casarsa,[48a] A. Castro,[6a,6b] P. Catastini,[20] D. Cauz,[48a,48b,48c] V. Cavaliere,[22] A. Cerri,[26,e] L. Cerrito,[28,r] Y. C. Chen,[1] M. Chertok,[7] G. Chiarelli,[41a] G. Chlachidze,[15] K. Cho,[25] D. Chokheli,[13] A. Clark,[18] C. Clarke,[52] M. E. Convery,[15] J. Conway,[7] M. Corbo,[15,z] M. Cordelli,[17] C. A. Cox,[7] D. J. Cox,[7] M. Cremonesi,[41a] D. Cruz,[47] J. Cuevas,[9,y] R. Culbertson,[15] N. d'Ascenzo,[15,v] M. Datta,[15,hh] P. de Barbaro,[44] L. Demortier,[45] M. Deninno,[6a] M. D'Errico,[39a,39b] F. Devoto,[21] A. Di Canto,[41a,41b] B. Di Ruzza,[15,p] J. R. Dittmann,[5] S. Donati,[41a,41b] M. D'Onofrio,[27] M. Dorigo,[48a,a48d] A. Driutti,[48a,48b,48c] K. Ebina,[51] R. Edgar,[31] R. Erbacher,[7] S. Errede,[22] B. Esham,[22] S. Farrington,[38] J. P. Fernández Ramos,[29] R. Field,[16] G. Flanagan,[15,t] R. Forrest,[7] M. Franklin,[20] J. C. Freeman,[15] H. Frisch,[11] Y. Funakoshi,[51] C. Galloni,[41a,41b] A. F. Garfinkel,[43] P. Garosi,[41a,41c] H. Gerberich,[22] E. Gerchtein,[15] S. Giagu,[46a] V. Giakoumopoulou,[3] K. Gibson,[42] C. M. Ginsburg,[15] N. Giokaris,[3] P. Giromini,[17] V. Glagolev,[13] D. Glenzinski,[15] M. Gold,[34] D. Goldin,[47] A. Golossanov,[15] G. Gomez,[9] G. Gomez-Ceballos,[30] M. Goncharov,[30] O. González López,[29] I. Gorelov,[34] A. T. Goshaw,[14] K. Goulianos,[45] E. Gramellini,[6a] C. Grosso-Pilcher,[11] J. Guimaraes da Costa,[20] S. R. Hahn,[15] J. Y. Han,[44] F. Happacher,[17] K. Hara,[49] M. Hare,[50] R. F. Harr,[52] T. Harrington-Taber,[15,m] M. Hartz,[42] K. Hatakeyama,[5] C. Hays,[38] J. Heinrich,[40] M. Herndon,[53] A. Hocker,[15] Z. Hong,[47] W. Hopkins,[15,f] S. Hou,[1] R. E. Hughes,[35] U. Husemann,[54] M. Hussein,[32,cc] J. Huston,[32] G. Introzzi,[41a,41e,41f] M. Iori,[46a,46b] A. Ivanov,[7,o] E. James,[15] D. Jang,[10] B. Jayatilaka,[15] E. J. Jeon,[25] S. Jindariani,[15] M. Jones,[43] K. K. Joo,[25] S. Y. Jun,[10] T. R. Junk,[15] M. Kambeitz,[24] T. Kamon,[25,47] P. E. Karchin,[52] A. Kasmi,[5] Y. Kato,[37,n] W. Ketchum,[11,ii] J. Keung,[40] B. Kilminster,[15,ee] D. H. Kim,[25] H. S. Kim,[15,bb] J. E. Kim,[25] M. J. Kim,[17] S. H. Kim,[49] S. B. Kim,[25] Y. J. Kim,[25] Y. K. Kim,[11] N. Kimura,[51] M. Kirby,[15] K. Knoepfel,[15] K. Kondo,[51,*] D. J. Kong,[25] J. Konigsberg,[16] A. V. Kotwal,[14] M. Kreps,[24] J. Kroll,[40] M. Kruse,[14] T. Kuhr,[24] M. Kurata,[49] A. T. Laasanen,[43] S. Lammel,[15] M. Lancaster,[28] K. Lannon,[35,x] G. Latino,[41a,41c] H. S. Lee,[25] J. S. Lee,[25] S. Leo,[22] S. Leone,[41a] J. D. Lewis,[15] A. Limosani,[14,s] E. Lipeles,[40] A. Lister,[18,a] Q. Liu,[43] T. Liu,[15] S. Lockwitz,[54] A. Loginov,[54] D. Lucchesi,[39a,39b] A. Lucà,[17] J. Lueck,[24] P. Lujan,[26] P. Lukens,[15] G. Lungu,[45] J. Lys,[26] R. Lysak,[12,d] R. Madrak,[15] P. Maestro,[41a,41c] S. Malik,[45] G. Manca,[27,b] A. Manousakis-Katsikakis,[3] L. Marchese,[6a,jj] F. Margaroli,[46a] P. Marino,[41a,41d] K. Matera,[22] M. E. Mattson,[52] A. Mazzacane,[15] P. Mazzanti,[6a] R. McNulty,[27,i] A. Mehta,[27] P. Mehtala,[21] C. Mesropian,[45] T. Miao,[15] D. Mietlicki,[31] A. Mitra,[1] H. Miyake,[49] S. Moed,[15] N. Moggi,[6a] C. S. Moon,[15,z] R. Moore,[15,ff,gg] M. J. Morello,[41a,41d] A. Mukherjee,[15] Th. Muller,[24] P. Murat,[15] M. Mussini,[6a,6b] J. Nachtman,[15,m] Y. Nagai,[49] J. Naganoma,[51] I. Nakano,[36] A. Napier,[50] J. Nett,[47] T. Nigmanov,[42] L. Nodulman,[2] S. Y. Noh,[25] O. Norniella,[22] L. Oakes,[38] S. H. Oh,[14] Y. D. Oh,[25] T. Okusawa,[37] R. Orava,[21] L. Ortolan,[4] C. Pagliarone,[48a] E. Palencia,[9,e] P. Palni,[34] V. Papadimitriou,[15] W. Parker,[53] G. Pauletta,[48a,48b,48c] M. Paulini,[10] C. Paus,[30] T. J. Phillips,[14] G. Piacentino,[15,q] E. Pianori,[40] J. Pilot,[7] K. Pitts,[22] C. Plager,[8] L. Pondrom,[53] S. Poprocki,[15,f] K. Potamianos,[26] A. Pranko,[26] F. Prokoshin,[13,aa] F. Ptohos,[17,g] G. Punzi,[41a,41b] I. Redondo Fernández,[29] P. Renton,[38] M. Rescigno,[46a] F. Rimondi,[6a,*] L. Ristori,[41a,15] A. Robson,[19] T. Rodriguez,[40] S. Rolli,[50,h] M. Ronzani,[41a,41b] R. Roser,[15] J. L. Rosner,[11] F. Ruffini,[41a,41c] A. Ruiz,[9] J. Russ,[10] V. Rusu,[15] W. K. Sakumoto,[44] Y. Sakurai,[51] L. Santi,[48a,48b,48c] K. Sato,[49] V. Saveliev,[15,v] A. Savoy-Navarro,[15,z] P. Schlabach,[15] E. E. Schmidt,[15] T. Schwarz,[31] L. Scodellaro,[9] F. Scuri,[41a] S. Seidel,[34] Y. Seiya,[37] A. Semenov,[13] F. Sforza,[41a,41b] S. Z. Shalhout,[7] T. Shears,[27] P. F. Shepard,[42] M. Shimojima,[49,u] M. Shochet,[11] I. Shreyber-Tecker,[33] A. Simonenko,[13] K. Sliwa,[50] J. R. Smith,[7] F. D. Snider,[15] H. Song,[42] V. Sorin,[4] R. St. Denis,[19,*] M. Stancari,[15] D. Stentz,[15,w] J. Strologas,[34] Y. Sudo,[49] A. Sukhanov,[15] I. Suslov,[13] K. Takemasa,[49] Y. Takeuchi,[49] J. Tang,[11] M. Tecchio,[31] P. K. Teng,[1] J. Thom,[15,f] E. Thomson,[40] V. Thukral,[47] D. Toback,[47] S. Tokar,[12] K. Tollefson,[32] T. Tomura,[49] D. Tonelli,[15,e] S. Torre,[17] D. Torretta,[15] P. Totaro,[39a] M. Trovato,[41a,41d] F. Ukegawa,[49] S. Uozumi,[25] F. Vázquez,[16,l] G. Velev,[15] C. Vellidis,[15] C. Vernieri,[41a,41d] M. Vidal,[43] R. Vilar,[9] J. Vizán,[9,dd] M. Vogel,[34] G. Volpi,[17] P. Wagner,[40] R. Wallny,[15,j] S. M. Wang,[1] D. Waters,[28] W. C. Wester III,[15] D. Whiteson,[40,c] A. B. Wicklund,[2] S. Wilbur,[7] H. H. Williams,[40] J. S. Wilson,[31] P. Wilson,[15] B. L. Winer,[35] P. Wittich,[15,f] S. Wolbers,[15] H. Wolfe,[35] T. Wright,[31] X. Wu,[18] Z. Wu,[5] K. Yamamoto,[37] D. Yamato,[37] T. Yang,[15] U. K. Yang,[25] Y. C. Yang,[25] W.-M. Yao,[26] G. P. Yeh,[15] K. Yi,[15,m] J. Yoh,[15] K. Yorita,[51] T. Yoshida,[37,k] G. B. Yu,[14] I. Yu,[25] A. M. Zanetti,[48a] Y. Zeng,[14] C. Zhou,[14] and S. Zucchelli[6a,6b]

(CDF Collaboration)

 © 2016 American Physical Society

[1]*Institute of Physics, Academia Sinica, Taipei, Taiwan 11529, Republic of China*
[2]*Argonne National Laboratory, Argonne, Illinois 60439, USA*
[3]*University of Athens, 157 71 Athens, Greece*
[4]*Institut de Fisica d'Altes Energies, ICREA, Universitat Autonoma de Barcelona, E-08193 Bellaterra (Barcelona), Spain*
[5]*Baylor University, Waco, Texas 76798, USA*
[6a]*Istituto Nazionale di Fisica Nucleare Bologna, I-40127 Bologna, Italy*
[6b]*University of Bologna, I-40127 Bologna, Italy*
[7]*University of California, Davis, Davis, California 95616, USA*
[8]*University of California, Los Angeles, Los Angeles, California 90024, USA*
[9]*Instituto de Fisica de Cantabria, CSIC-University of Cantabria, 39005 Santander, Spain*
[10]*Carnegie Mellon University, Pittsburgh, Pennsylvania 15213, USA*
[11]*Enrico Fermi Institute, University of Chicago, Chicago, Illinois 60637, USA*
[12]*Comenius University, 842 48 Bratislava, Slovakia; Institute of Experimental Physics, 040 01 Kosice, Slovakia*
[13]*Joint Institute for Nuclear Research, RU-141980 Dubna, Russia*
[14]*Duke University, Durham, North Carolina 27708, USA*
[15]*Fermi National Accelerator Laboratory, Batavia, Illinois 60510, USA*
[16]*University of Florida, Gainesville, Florida 32611, USA*
[17]*Laboratori Nazionali di Frascati, Istituto Nazionale di Fisica Nucleare, I-00044 Frascati, Italy*
[18]*University of Geneva, CH-1211 Geneva 4, Switzerland*
[19]*Glasgow University, Glasgow G12 8QQ, United Kingdom*
[20]*Harvard University, Cambridge, Massachusetts 02138, USA*
[21]*Division of High Energy Physics, Department of Physics, University of Helsinki, Helsinki FIN-00014, Finland; Helsinki Institute of Physics, Helsinki FIN-00014, Finland*
[22]*University of Illinois, Urbana, Illinois 61801, USA*
[23]*The Johns Hopkins University, Baltimore, Maryland 21218, USA*
[24]*Institut für Experimentelle Kernphysik, Karlsruhe Institute of Technology, D-76131 Karlsruhe, Germany*
[25]*Center for High Energy Physics: Kyungpook National University, Daegu 702-701, Korea; Seoul National University, Seoul 151-742, Korea; Sungkyunkwan University, Suwon 440-746, Korea; Korea Institute of Science and Technology Information, Daejeon 305-806, Korea; Chonnam National University, Gwangju 500-757, Korea; Chonbuk National University, Jeonju 561-756, Korea; Ewha Womans University, Seoul 120-750, Korea*
[26]*Ernest Orlando Lawrence Berkeley National Laboratory, Berkeley, California 94720, USA*
[27]*University of Liverpool, Liverpool L69 7ZE, United Kingdom*
[28]*University College London, London WC1E 6BT, United Kingdom*
[29]*Centro de Investigaciones Energeticas Medioambientales y Tecnologicas, E-28040 Madrid, Spain*
[30]*Massachusetts Institute of Technology, Cambridge, Massachusetts 02139, USA*
[31]*University of Michigan, Ann Arbor, Michigan 48109, USA*
[32]*Michigan State University, East Lansing, Michigan 48824, USA*
[33]*Institution for Theoretical and Experimental Physics, ITEP, Moscow 117259, Russia*
[34]*University of New Mexico, Albuquerque, New Mexico 87131, USA*
[35]*The Ohio State University, Columbus, Ohio 43210, USA*
[36]*Okayama University, Okayama 700-8530, Japan*
[37]*Osaka City University, Osaka 558-8585, Japan*
[38]*University of Oxford, Oxford OX1 3RH, United Kingdom*
[39a]*Istituto Nazionale di Fisica Nucleare, Sezione di Padova, I-35131 Padova, Italy*
[39b]*University of Padova, I-35131 Padova, Italy*
[40]*University of Pennsylvania, Philadelphia, Pennsylvania 19104, USA*
[41a]*Istituto Nazionale di Fisica Nucleare Pisa, I-27100 Pavia, Italy*
[41b]*University of Pisa, I-27100 Pavia, Italy*
[41c]*University of Siena, I-27100 Pavia, Italy*
[41d]*Scuola Normale Superiore, I-56127 Pisa, Italy*
[41e]*INFN Pavia, I-27100 Pavia, Italy*
[41f]*University of Pavia, I-27100 Pavia, Italy*
[42]*University of Pittsburgh, Pittsburgh, Pennsylvania 15260, USA*
[43]*Purdue University, West Lafayette, Indiana 47907, USA*
[44]*University of Rochester, Rochester, New York 14627, USA*
[45]*The Rockefeller University, New York, New York 10065, USA*
[46a]*Istituto Nazionale di Fisica Nucleare, Sezione di Roma 1, I-00185 Roma, Italy*

[46b]*Sapienza Università di Roma, I-00185 Roma, Italy*
[47]*Mitchell Institute for Fundamental Physics and Astronomy, Texas A&M University, College Station, Texas 77843, USA*
[48a]*Istituto Nazionale di Fisica Nucleare Trieste, I-33100 Udine, Italy*
[48b]*Gruppo Collegato di Udine, I-33100 Udine, Italy*
[48c]*University of Udine, I-33100 Udine, Italy*
[48d]*University of Trieste, I-34127 Trieste, Italy*
[49]*University of Tsukuba, Tsukuba, Ibaraki 305, Japan*
[50]*Tufts University, Medford, Massachusetts 02155, USA*
[51]*Waseda University, Tokyo 169, Japan*
[52]*Wayne State University, Detroit, Michigan 48201, USA*
[53]*University of Wisconsin-Madison, Madison, Wisconsin 53706, USA*
[54]*Yale University, New Haven, Connecticut 06520, USA*
(Received 17 January 2016; published 1 March 2016)

We describe a measurement of the ratio of the cross sections times branching fractions of the B_c^+ meson in the decay mode $B_c^+ \to J/\psi\mu^+\nu$ to the B^+ meson in the decay mode $B^+ \to J/\psi K^+$ in proton-antiproton collisions at center-of-mass energy $\sqrt{s} = 1.96$ TeV. The measurement is based on the complete CDF Run II data set, which comes from an integrated luminosity of 8.7 fb^{-1}. The ratio of the production cross sections times branching fractions for B_c^+ and B^+ mesons with momentum transverse to the beam greater than 6 GeV/c and rapidity magnitude smaller than 0.6 is $0.211 \pm 0.012(\text{stat})^{+0.021}_{-0.020}(\text{syst})$. Using the known $B^+ \to J/\psi K^+$ branching fraction, the known B^+ production cross section, and a selection of the predicted $B_c^+ \to J/\psi\mu^+\nu$ branching fractions, the range for the total B_c^+ production cross section is estimated.

DOI: 10.1103/PhysRevD.93.052001

[*]Deceased.
[a]Visitor from University of British Columbia, Vancouver, BC V6T 1Z1, Canada.
[b]Visitor from Istituto Nazionale di Fisica Nucleare, Sezione di Cagliari, 09042 Monserrato (Cagliari), Italy.
[c]Visitor from University of California Irvine, Irvine, CA 92697, USA.
[d]Visitor from Institute of Physics, Academy of Sciences of the Czech Republic, 182 21, Czech Republic.
[e]Visitor from CERN, CH-1211 Geneva, Switzerland.
[f]Visitor from Cornell University, Ithaca, NY 14853, USA.
[g]Visitor from University of Cyprus, Nicosia CY-1678, Cyprus.
[h]Visitor from Office of Science, U.S. Department of Energy, Washington, D.C. 20585, USA.
[i]Visitor from University College Dublin, Dublin 4, Ireland.
[j]Visitor from ETH, 8092 Zürich, Switzerland.
[k]Visitor from University of Fukui, Fukui City, Fukui Prefecture 910-0017, Japan.
[l]Visitor from Universidad Iberoamericana, Lomas de Santa Fe, C.P. 01219, Distrito Federal, México.
[m]Visitor from University of Iowa, Iowa City, IA 52242, USA.
[n]Visitor from Kinki University, 577-8502 Higashi-Osaka City, Japan.
[o]Visitor from Kansas State University, Manhattan, KS 66506, USA.
[p]Visitor from Brookhaven National Laboratory, Upton, NY 11973, USA.
[q]Visitor from Istituto Nazionale di Fisica Nucleare, Sezione di Lecce, Via Arnesano, I-73100 Lecce, Italy.
[r]Visitor from Queen Mary, University of London, London E1 4NS, United Kingdom.
[s]Visitor from University of Melbourne, Victoria 3010, Australia.
[t]Visitor from Muons, Inc., Batavia, IL 60510, USA.
[u]Visitor from Nagasaki Institute of Applied Science, Nagasaki 851-0193, Japan.
[v]Visitor from National Research Nuclear University, Moscow 115409, Russia.
[w]Visitor from Northwestern University, Evanston, IL 60208, USA.
[x]Visitor from University of Notre Dame, Notre Dame, IN 46556, USA.
[y]Visitor from Universidad de Oviedo, E-33007 Oviedo, Spain.
[z]Visitor from CNRS-IN2P3, Paris F-75205, France.
[aa]Visitor from Universidad Tecnica Federico Santa Maria, 110v Valparaiso, Chile.
[bb]Visitor from Sejong University, Seoul 143-747, Korea.
[cc]Visitor from The University of Jordan, Amman 11942, Jordan.
[dd]Visitor from Universite catholique de Louvain, 1348 Louvain-La-Neuve, Belgium.
[ee]Visitor from University of Zürich, 8006 Zürich, Switzerland.
[ff]Visitor from Massachusetts General Hospital, Boston, MA 02114 USA.
[gg]Visitor from Harvard Medical School, Boston, MA 02114 USA.
[hh]Visitor from Hampton University, Hampton, VA 23668, USA.
[ii]Visitor from Los Alamos National Laboratory, Los Alamos, NM 87544, USA.
[jj]Visitor from Università degli Studi di Napoli Federico I, I-80138 Napoli, Italy.

I. INTRODUCTION

We report a measurement of the ratio of the production cross sections times branching fractions (BF)

$$\mathcal{R} = \frac{\sigma(B_c^+)\mathcal{B}(B_c^+ \to J/\psi\mu^+\nu)}{\sigma(B^+)\mathcal{B}(B^+ \to J/\psi K^+)} \tag{1}$$

in proton-antiproton ($p\bar{p}$) collisions at a center-of-mass energy of 1.96 TeV measured using the full CDF data set collected from February of 2001 through September of 2011 (Run II), which comes from an integrated luminosity of 8.7 fb^{-1}.

The B_c^+-meson [1] production cross section is predicted to be three orders of magnitude smaller than the B^+-meson production cross section [2,3]. The branching fraction of the $B^+ \to J/\psi K^+$ decay is $(1.027 \pm 0.031) \times 10^{-3}$ [4], while the branching fraction of the $B_c^+ \to J/\psi\mu^+\nu$ is predicted to be approximately 2% [5,6]. Thus, we expect $\mathcal{R}$ to be $\mathcal{O}(10^{-2})$.

The B_c^+ meson, with a mass of 6.2756 ± 0.0011 GeV/c^2 [4], is the most massive meson involving unlike-quark flavors, with a ground state consisting of a $\bar{b}$ and a c quark. Both the b and c quarks decay through the weak interaction and, unlike in $c\bar{c}$ and $b\bar{b}$ quarkonia, cannot annihilate into gluons. Consequently, there are many possible final states to explore new aspects of heavy-quark dynamics. Studies of strong-interaction B_c^+ production have been possible only at hadron colliders because of the low center-of-mass energy at e^+e^- colliders operating at the $\Upsilon(4S)$ resonance and the small $q\bar{q}$ cross section in e^+e^- collisions at the Z resonance. The CDF II detector features significant improvements in the system for reconstructing charged-particle trajectories (tracking) that increase the acceptance and facilitate the detection and precise measurement of the kinematic properties of b hadrons and their decay products. Together with the increased luminosity, this makes it possible to measure more precisely the properties of the B_c^+ meson with the significantly larger samples of B hadrons collected in Run II.

Since the production cross section of the B^+-meson and its branching fraction in the decay channel $B^+ \to J/\psi K^+$ are well measured, it is convenient to measure the B_c^+ production cross section with the $B_c^+ \to J/\psi\mu^+\nu$ channel using the kinematically similar $B^+ \to J/\psi K^+$ channel as a reference. Many systematic effects related to detector and online-event-selection (trigger) efficiencies are expected to cancel in the ratio $\mathcal{R}$, given that the event topologies are similar and all J/ψ candidates in either the $B_c^+ \to J/\psi\mu^+\nu$ or the $B^+ \to J/\psi K^+$ final state are reconstructed using a common set of trigger criteria.

Both the B^+ and B_c^+ production cross sections include production from excited B states that subsequently decay into B^+ or B_c^+ mesons. Excited B^+ states that contribute to the B^+ ground state include the radiative decay $B^{*+} \to B^+\gamma$, as well as orbital excitations of the B^+ and B^0 mesons, e.g., $B^{**0} \to B^{+(*)}\pi^-$. In the case of the B_c^+ meson, besides direct production of the ground state, contributions are only allowed from excited states of the B_c^+ meson itself because of flavor conservation. Therefore, any excited B_c^+ state whose mass is smaller than the sum of the bottom and charm meson masses cascades into the B_c^+ ground state, primarily through radiative decay. For example, the production cross section of the B_c^{*+} meson [2] is estimated to be approximately 2.5 times the cross section to the ground state B_c^+, and the B_c^{*+} meson reaches the ground state through the radiative decay $B_c^{*+} \to B_c^+\gamma$, where the mass splitting between the B_c^{*+} and B_c^+ mesons is estimated to be within the range 40–76 MeV/c^2 [7]. Less important are the P-wave excited $B_{cJ,L=1}^{*+}$ states whose total cross section is estimated to be about 1/2 of that of direct production to the ground state B_c^+ [8].

The ratio $\mathcal{R}$ can be measured using the formula

$$\mathcal{R} = \frac{N_{B_c^+}}{N_{B^+}} \frac{\epsilon_{B^+}}{\epsilon_{B_c^+}} \frac{1}{\epsilon_\mu}, \tag{2}$$

where $N_{B_c^+}$ and N_{B^+} are the numbers of reconstructed $B_c^+ \to J/\psi\mu^+\nu$ and $B^+ \to J/\psi K^+$ events estimated in experimental data after all background subtractions and other corrections, respectively; ϵ_{B^+} and $\epsilon_{B_c^+}$ are the total efficiencies for selecting and reconstructing the decays $B^+ \to J/\psi K^+$ and $B_c^+ \to J/\psi\mu^+\nu$, respectively; and ϵ_μ is the muon identification efficiency. On the right side of Eq. (2), the first factor is the relative yield for the two decays, the second term gives the scaling for the relative geometrical acceptance and detection efficiency, and the third term is a correction for the muon efficiency relative to kaons. The overall relative efficiency $\epsilon_{\rm rel}$ is defined by $\epsilon_{\rm rel} = \epsilon_{B^+}/(\epsilon_{B_c^+} \times \epsilon_\mu)$. The selection criteria for both B_c^+ and B^+ events are made as nearly identical as possible to minimize systematic uncertainties in both the relative yields and in determining $\epsilon_{\rm rel}$.

The number of $B^+ \to J/\psi K^+$ decays is determined from a fit to the invariant-mass spectrum around the known B^+ mass value, which includes a background component, a signal component, and a correction for the Cabibbo-suppressed $J/\psi\pi^+$ final state. Since the B_c^+ decay is only partially reconstructed, the number of $B_c^+ \to J/\psi\mu^+\nu$ candidates is determined by counting the total number of $J/\psi\mu^+$ events in the invariant-mass window $4\ \text{GeV}/c^2 < M(J/\psi\mu^+) < 6\ \text{GeV}/c^2$ and subtracting the contributions of known backgrounds. The quantity $M(J/\psi\mu^+)$ is the invariant mass of the trimuon partial reconstruction of the $J/\psi\mu^+X$ final state, where X represents any undetected particles. Because the signal events are spread over a 2 GeV/c^2 invariant-mass interval, the background cannot be determined by a simple sideband subtraction. A large fraction of this paper is devoted to describing the methods used to determine the various backgrounds included in the $B_c^+ \to J/\psi\mu^+\nu$ candidate

sample. The principal classes of background events are the following: a wrongly identified or misidentified-J/ψ candidate with a real third muon, a real J/ψ meson with a wrongly identified or misidentified third muon, and a real J/ψ meson with a real muon that originated from different b quarks in the same event. These backgrounds are determined quantitatively from independent data samples wherever possible and from Monte Carlo (MC) simulation otherwise. We correct for misidentified-J/ψ candidates with misidentified muons that are contained in two of the major backgrounds above and for backgrounds from other B_c^+ decay modes that yield a $J/\psi\mu^+X$ final state (for examples see Table XI in Sec. V). The analysis demonstrates that about half of the inclusive $J/\psi\mu^+X$ sample is $B_c^+ \to J/\psi\mu^+\nu$ events, and the remainder is background with a small contribution from other B_c^+ decay modes.

Because the signal events are confined to a 2 GeV/c^2 mass region between 4 and 6 GeV/c^2, we use the events at masses between 3 and 4 GeV/c^2 and greater than 6 GeV/c^2 as a control sample to check the predictions for the major backgrounds in the signal region.

The elements of the CDF II detector most relevant to this analysis are discussed in Sec. II. The selection of B_c^+ and B^+ candidates is described in Sec. III. Backgrounds are described in Sec. IV. Contributions from other B_c^+ decays are estimated in Sec. V, and the final corrected $B_c^+ \to J/\psi\mu^+\nu$ signal is discussed in Sec. VI. Since the measurement of $B_c^+ \to J/\psi\mu^+\nu$ is made relative to the decay $B^+ \to J/\psi K^+$, the relative reconstruction efficiency of the two decay modes in the CDF II detector is estimated using MC simulation, which is described in Sec. VII. Systematic uncertainties assigned to the measurement are described throughout the paper. Final results are presented in Sec. VIII.

II. CDF II DETECTOR DESCRIPTION

The CDF II detector is a multipurpose, nearly cylindrically symmetric detector consisting of a collection of silicon-strip detectors, a drift chamber, and a time-of-flight (ToF) detector immersed in a 1.4 T solenoidal magnetic field, surrounded by electromagnetic and hadronic calorimeters with a projective-tower geometry, and followed by absorber and wire-chamber muon detectors. The apparatus is described in more detail in Refs. [9,10].

Because the CDF II detector has a nearly azimuthally symmetric geometry that extends along the $p\bar{p}$ beam axis, the detector is described with a cylindrical coordinate system in which ϕ is the azimuthal angle, r is the radial distance from the nominal beam line, and z points in the proton-beam direction with the origin at the center of the detector. The transverse r-ϕ or x-y plane is the plane perpendicular to the z axis. The pseudorapidity η is defined in terms of the polar angle θ by $\eta = -\ln[\tan(\theta/2)]$, where $\theta = 0$ corresponds to the proton direction. The transverse momentum p_T of a particle is given by $p_T = p\sin(\theta)$ where p is the magnitude of the particle momentum.

A. Charged-particle trajectories

Charged-particle trajectories (tracks) are measured in the CDF II detector by a combination of silicon-strip detectors and a drift chamber called the central outer tracker (COT). The two innermost components of the charged-particle-tracking system used in this analysis are the silicon vertex detector (SVX II) [11,12] with five double-sided layers with r between 2.5 and 10.6 cm, and the intermediate silicon layers (ISL) [12,13] with three double-sided partial layers with r between 20 and 29 cm.

The five layers of the SVX II are arranged in five cylindrical shells and divided into three identical sections (barrels) along the beam axis for a total z coverage of 90 cm excluding gaps. Each barrel is divided into 12 azimuthal wedges of 30° as illustrated in Fig. 1, which shows an r-ϕ slice of the SVX II. The sensors have strip pitches ranging from 60 to 140 μm depending on the radius. They have strips on both sides of the silicon to allow for two position measurements at each layer. All layers have axial strips parallel to the beam direction for ϕ measurements. Three layers have strips perpendicular to the beam direction to measure z position, while the remaining two layers have strips that are tilted by 1.2° relative to the axial strips.

The ISL detector serves to extend the precision of the SVX II to larger radius and allows for better matching of tracking information between the silicon detectors and the COT. The ISL sensors are double sided with axial and 1.2° strips spaced with a pitch of 112 μm.

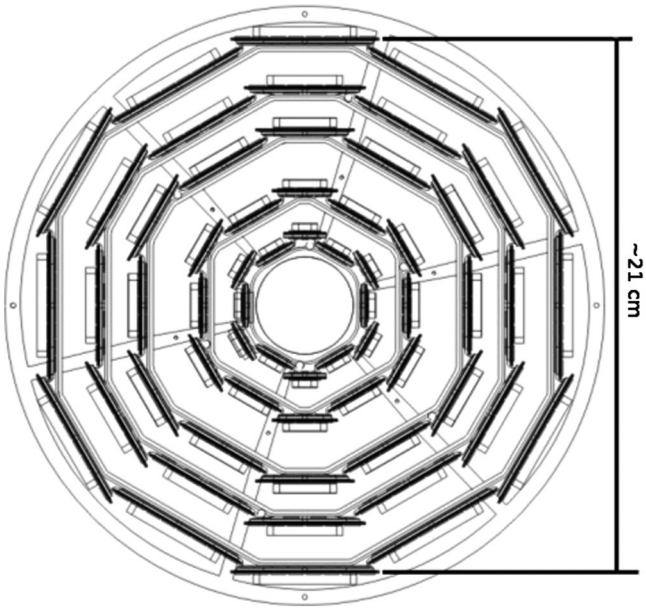

FIG. 1. Arrangement of sensors in the five SVX II layers in an r-ϕ slice.

The silicon detectors provide a precise measurement of the azimuth of tracks and of their transverse impact parameter, the distance by which trajectories extrapolated back in the r-ϕ plane miss the beam line. For particles with $p_T = 2$ GeV/c, the transverse-impact-parameter resolution given by the SVX II is about 50 μm; this includes a contribution of approximately 30 μm due to the transverse beam-spot size [12]. In this analysis the silicon detectors provide precise measurements of the decay vertices for B_c^+ and B^+ candidates.

The 310 cm long COT [14] is an open-cell multiwire proportional drift chamber consisting of 96 sense-wire layers from $r = 40$ cm to $r = 137$ cm. The layers are grouped into alternating axial and $\pm 2°$ stereo superlayers. The relative positions of the silicon and COT tracking systems are shown in Fig. 2. The COT alone provides excellent track reconstruction and momentum resolution. For the combined COT, ISL, and SVX II tracking system, the asymptotic transverse momentum resolution $\delta p_T/p_T$ has a p_T dependence given by $\delta p_T/p_T = 0.0007 p_T(\mathrm{GeV/c})$. In addition the COT provides sampling of the specific-ionization-energy loss dE/dx along a track, which provides particle-type identification [15].

Following the COT in radius, but located inside the solenoid coil, is a ToF detector [16] consisting of scintillator bars with photomultiplier tubes at both ends. The ToF system has a resolution of approximately 110 ps [17] that corresponds to a separation of 0.6σ between pions and kaons at $p = 3$ GeV/c. Both the ToF and dE/dx measurements are important in determining the particle fractions in the analysis of the misidentified-muon background discussed in Sec. IV B.

B. Muon detectors

The central muon detector (CMU) [18] consists of single-wire drift cells located outside of each calorimeter wedge, covering $|\eta| < 0.6$, starting at $r = 347$ cm. For particle trajectories at 90°, there are approximately 5.5 interaction lengths for hadron attenuation before the wire drift cells. The drift cell arrays sample the trajectories in up to four positions in the r-ϕ plane that are used to form straight track segments. The track segments are matched to extrapolated COT tracks to form muon candidates using both position and slope.

The central muon upgrade detector (CMP) covers the same $|\eta| < 0.6$ range as the CMU. Arranged in a box that surrounds the central region of the detector, the CMP consists of single-wire drift cells stacked in four layers similar to the CMU. Since the CMP is located behind an additional 60 cm of steel (approximately 3.3 interaction lengths), there are considerably fewer kaons and pions that penetrate to the CMP compared to the CMU. Muon candidates associated with track segments in both the CMU and CMP are called CMUP muons.

The central muon extension detector (CMX) extends the muon coverage to the kinematic region $0.6 < |\eta| < 1.0$. The CMX consists of eight layers of single-wire drift tubes. The calorimeter, together with detector supports, provides approximately 6 (at $\eta = 0.6$) to 10 (at $\eta = 1.1$) interaction lengths of absorber in front of the CMX for hadron attenuation [19].

This analysis uses the CMU and CMX to identify the muon candidates for reconstructing J/ψ mesons, but requires the CMUP for the third muon in the semileptonic decay $B_c^+ \to J/\psi\mu^+X$.

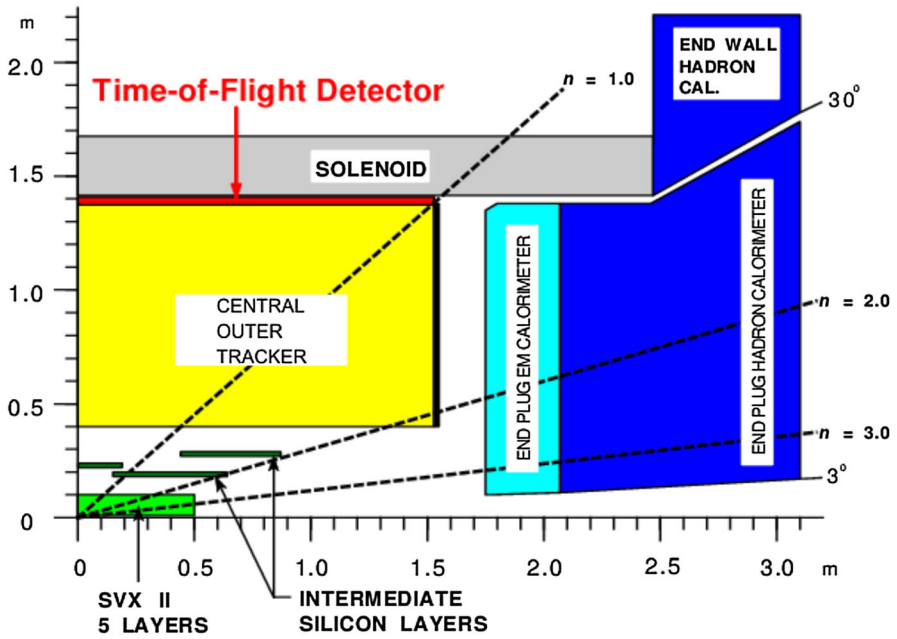

FIG. 2. One quarter r-z side view of the COT showing its position relative to other detectors.

C. Online event-selection system

The Tevatron average beam crossing rate is 1.7 MHz, and the typical CDF II triggered event size is about 300 kB. Since the data-acquisition system can write about 20 MB/s to permanent storage, it is necessary to reject 99.996% of the $p\bar{p}$ collisions. This is accomplished by a three-level online event-selection system (trigger). The first two levels use custom electronic logic circuits to choose or reject events and the third level uses a parallel array of commodity personal computers.

The level-1 trigger makes decisions using information from the COT, calorimeters, and muon detectors. The extremely fast tracker (XFT) [20], a pattern-recognition system for fast COT track reconstruction, provides the tracks for the level-1 trigger [21]. The decision time is fixed at 5.5 μs and this requires a pipeline buffer with a depth of 42 events for the storage of event data while decisions are made. The typical level-1 rate of event acceptance is approximately 20 kHz. For this analysis events are collected by one of two level-1 triggers: two XFT tracks corresponding to charged particles with $p_T > 1.5$ GeV/c are matched with track segments in the CMU detector, or one XFT track corresponding to a particle with $p_T > 1.5$ GeV/c is matched with a CMU track segment, while another with $p_T > 2.0$ GeV/c is matched with a CMX track segment.

After an event is accepted by the level-1 trigger, it is passed to the level-2 trigger [22]. The level-2 trigger uses the same information as the level-1 trigger with additional track position information from the silicon vertex trigger (SVT). The SVT applies pattern recognition to SVX II silicon hits (a positive detector response to the passage of a charged particle) that are matched to XFT tracks and calculates impact parameters for the tracks [23]. Events with track vertices (two or more tracks originating from a common point) displaced from the beam line, i.e., likely to contain the decay of a long-lived particle such as a B or D meson, are chosen by requiring two SVT tracks with nonzero impact parameters. For the case of the dimuon triggers used to collect signal candidates for this analysis, the SVT is not used, but SVT-triggered events are used to reconstruct control samples used in the analysis, such as $D^{*+} \to D^0\pi^+$ followed by $D^0 \to K^-\pi^+$. These decays are used to define cleanly identified samples of pions and kaons to measure the probabilities that such hadrons are misidentified as muons. The level-2 trigger typically has a total output rate of 200–800 Hz.

The level-3 trigger system [24] uses information from all parts of the CDF II detector to reconstruct and select events. The typical output rate for level 3 is approximately 100 Hz. For the level-3-J/ψ trigger used in this analysis, there is a selection on the J/ψ that requires the invariant mass of the muon pair used in the reconstruction to fall in the range 2.7–4.0 GeV/c^2.

III. EVENT SELECTION

The high spatial resolution provided by the silicon-tracking system in the plane transverse to the beam line makes it ideal for the reconstruction of B hadrons. Because tracks curve in the transverse plane, the transverse momentum is well measured. Additionally, the small transverse $p\bar{p}$ interaction region constrains the location of the $p\bar{p}$ collision space point (primary vertex) in this plane. Consequently, we use the transverse momentum p_T of the reconstructed hadron and transverse decay length L_{xy}, which is the decay length of the reconstructed three-track system projected into the transverse plane, when selecting B_c^+ and B^+ candidates and when discriminating against backgrounds. Unless otherwise noted, L_{xy} is measured from the primary vertex of the event to the candidate B-meson decay point (decay vertex).

We use similar selection requirements for both the $B_c^+ \to J/\psi\mu^+X$ and $B^+ \to J/\psi K^+$ decays to minimize possible systematic uncertainties in the relative efficiency between the two modes.

A. $J/\psi \to \mu^+\mu^-$ selection

The data are collected with a dimuon trigger that requires two oppositely charged muon candidates (see Sec. II C). The trigger requirements are confirmed in our offline analysis using track variables reconstructed from track fits for track candidates passing our selection criteria. To guarantee good track quality, each track is required to have at least three r-ϕ hits in the silicon detector and hits in at least ten axial and ten stereo layers in the COT. We define a likelihood ratio $\mathcal{L}R(\mu)$ that incorporates information from the muon detectors, calorimeters, and tracking detectors to optimize the separation of real muons from hadrons [25]. This muon likelihood selection is determined from an optimization study carried out on the signal and sideband regions of the $\mu^+\mu^-$ invariant-mass distribution [26]. The dimuon invariant-mass distribution near the J/ψ-meson mass with muon candidates that satisfy the muon likelihood selection is shown in Fig. 3. In the J/ψ signal region, there are 6.1×10^7 dimuon events. Selection of the J/ψ meson requires the two muons to come from a common decay point and have an invariant mass that lies within 50 MeV/c^2 of the known J/ψ-meson mass [4]. The selection requirements applied to the $J/\psi \to \mu^+\mu^-$ candidates are listed in Table I.

B. Three-track-system selection

The three-track event candidates used in this analysis are chosen by matching a third track to a J/ψ candidate in three dimensions, where the χ^2 probability for the kinematic fit to a common vertex is greater than 0.001 with the dimuons from the J/ψ decay constrained to the known invariant mass of the J/ψ meson [4]. The selection requirements used to choose the sample of three tracks consistent with a

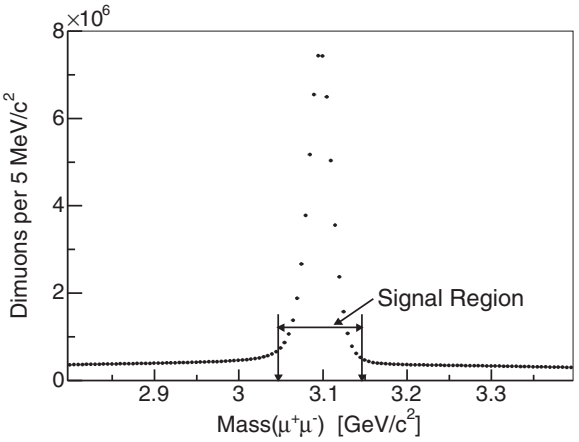

FIG. 3. Dimuon invariant-mass distribution for oppositely charged muon pairs near the J/ψ-meson mass. The signal region for selecting a J/ψ meson is shown.

common origin are listed in Table II. The three-track sample is also called the J/ψ-track sample and is the sample from which decays $B_c^+ \to J/\psi\mu^+X$ and $B^+ \to J/\psi K^+$ are reconstructed. Candidates for the $B_c^+ \to J/\psi\mu^+\nu$ decay are chosen by requiring the third track to be identified as a muon in both the CMU and CMP detectors (CMUP) as described in Sec. II B. In addition to the continuum background that contributes to the $B^+ \to J/\psi K^+$ decay candidates, there is the Cabibbo-suppressed decay $B^+ \to J/\psi\pi^+$. Background to $B_c^+ \to J/\psi\mu^+X$ decays arises when a π^+, K^+, or p is misidentified as a muon (misidentified-muon background). Another background is contributed when a real muon from one B-hadron decay combined with a real J/ψ candidate from a different B-hadron decay passes the three-track vertex-selection requirements ($b\bar{b}$ background). The J/ψ-track sample is used extensively to determine the rate of hadrons producing muon signatures in the detector (see Sec. IV B). The third, fourth, and fifth columns in Table II identify which selection criteria are applied to the B_c^+, B^+, and J/ψ-track candidates, respectively.

TABLE I. Selection requirements applied to the muons of J/ψ candidates and to the two-particle J/ψ candidates. The two muons are labeled μ_1 and μ_2 to identify the two tracks of the trigger.

Selection requirement	Value
μ_1	$\lvert\eta\rvert < 0.6$ and $p_T > 1.5$ GeV/c
μ_2	($\lvert\eta\rvert < 0.6$ and $p_T > 1.5$ GeV/c) or ($0.6 \le \lvert\eta\rvert < 1.0$ and $p_T > 2.0$ GeV/c)
COT hits/track	Hits in ten axial and ten stereo layers
r-ϕ silicon hits/track	≥ 3
Muon likelihood/muon	Optimized using likelihood ratio
$\lvert M(\mu_1\mu_2) - M_{J/\psi}\rvert$	<50.0 MeV/c^2

The CMUP requirement is not made for the B^+ or J/ψ-track samples. However, to ensure that the acceptance is consistent across samples, the third track is required to extrapolate to the same region of the CMU and CMP detectors as the third-muon candidates and to satisfy the isolation cut applied to third-muon candidates. In all three samples the third track is required to meet the XFT criteria because the events of the control sample used to determine the probabilities that pions and kaons are misidentified as muons (see Sec. IV B) are selected with the XFT trigger. The muon selection also requires that no other track with $p_T > 1.45$ GeV/c extrapolates to within a transverse distance of 40 cm in the r-ϕ plane at the front face of the CMU element relative to the track candidate observed. This "track isolation requirement" ensures that the estimation of the misidentified-muon background is consistent across the various data samples used in the analysis and does not require a correction for local track density.

To penetrate the additional absorber between the CMU and CMP detectors, a muon must have a minimum initial transverse momentum greater than 3 GeV/c. Consequently, the third track in all three samples is required to have a transverse momentum greater than 3 GeV/c. To ensure good-quality track reconstruction in all samples, standard criteria (see Table II) for good track and vertex reconstruction and reliable dE/dx information are imposed.

The azimuthal opening angle ϕ in the lab frame between the J/ψ and third track is required to be less than $\pi/2$ in all samples because no signal events are expected to contribute outside of this azimuthal aperture. The uncertainty $\sigma_{L_{xy}}$ on L_{xy} is required to be less than 200 μm in the transverse plane. Simulation studies indicate that this requirement removes primarily background events and a negligible number of signal events. The selection criterion $L_{xy}/\sigma_{L_{xy}} > 3$ is chosen to eliminate the prompt J/ψ background that arises from J/ψ mesons produced directly in the $p\bar{p}$ interaction. The invariant masses of events in the $J/\psi\mu^+$ and J/ψ-track samples are reconstructed with the mass of the third charged particle assigned as a pion, kaon, or muon mass, depending on how the event is used in the analysis. The signal region for $B_c^+ \to J/\psi\mu^+\nu$ candidates is set between 4 and 6 GeV/c^2. In the $J/\psi\mu^+$ sample the mass of the third charged particle is normally assumed to be that of a muon, but to eliminate residual $B^+ \to J/\psi K^+$ background, we remove all events with an invariant mass within 50 MeV/c^2 of the known value of the B^+ mass [4] assuming the mass of the third particle to be that of a kaon.

Using the $J/\psi \to \mu^+\mu^-$ selection requirements from Table I and the B_c^+ and B^+ selection requirements from Table II, the invariant-mass distributions of the $J/\psi\mu^+$ and $J/\psi K^+$ candidates are constructed. These are shown in Fig. 4. Both samples are subsets of the J/ψ-track sample

TABLE II. Selection requirements applied to the third track and the three-particle J/ψ-track system and samples selected from the J/ψ-track system.

Selection requirement	Value	B_c^+	B^+	J/ψ-track
	Third track			
Muon type	CMUP	X		
CMUP boundary	Track extrapolates to CMU and CMP detectors	X	X	X
Match with XFT	Track is required to trigger XFT	X	X	X
Isolation at CMU	No other extrapolated track within 40 cm at CMU	X	X	X
p_T	>3.0 GeV$/c$	X	X	X
r-ϕ silicon hits/track	≥ 3	X	X	X
COT hits/track	Ten stereo and ten axial hits	X	X	X
dE/dx hits/track	≥ 43 hits	X	X	X
	J/ψ-track system			
Kinematic-fit probability	>0.001	X	X	X
$\Delta\phi$	$<\pi/2$	X	X	X
$\sigma_{L_{xy}}$	<200 μm	X	X	X
$L_{xy}/\sigma_{L_{xy}}$	>3	X	X	X
B_c^+ mass region	$\lvert M(J/\psi\text{track}) - 5.0\ \text{GeV}/c^2\rvert < 1.0\ \text{GeV}/c^2$	X		X
$J/\psi K^+$ mass Veto	$\lvert M(J/\psi K^+) - 5.279\ \text{GeV}/c^2\rvert > 0.05\ \text{GeV}/c^2$	X		X

and must pass a minimum $p_T > 6$ GeV$/c$ requirement applied to the three-track system, where the third track is assumed to be either a muon or kaon, depending on the sample.

We select 1370 ± 37 $J/\psi\mu^+$ candidate events within a 4–6 GeV$/c^2$ signal mass window. To extract the number of $B^+ \to J/\psi K^+$ events, the $J/\psi K^+$ invariant-mass distribution is fit with a function that consists of a double Gaussian for $B^+ \to J/\psi K^+$ decays, a template for the invariant-mass distribution generated by MC simulation for the Cabibbo-suppressed $B^+ \to J/\psi\pi^+$ contribution within the mass range 5.28–5.4 GeV$/c^2$, and a second-order polynomial for the continuum background. The Cabibbo-suppressed $B^+ \to J/\psi\pi^+$ contribution is fixed to 3.83% of the number of $B^+ \to J/\psi K^+$ decays following Ref. [27]. The fit determines a yield of $14\,338 \pm 125$ $B^+ \to J/\psi K^+$ decays.

IV. B_c^+ BACKGROUNDS

We consider contributions to the B_c^+ backgrounds from events in which a J/ψ candidate is misidentified, a third muon is misidentified, or $b\bar{b}$ pairs decay in which one of the b quarks produces the J/ψ meson and the other produces the third muon. The misidentified-J/ψ-meson background is due to the reconstruction of a $J/\psi \to \mu^+\mu^-$ candidate that does not consist of real muons originating from a J/ψ meson, but from hadrons incorrectly identified as muons that produce a mass consistent with that of the J/ψ meson. This background is estimated from the sidebands of the $\mu^+\mu^-$ invariant-mass distribution and is discussed in Sec. IV A. The misidentified-muon background is due to

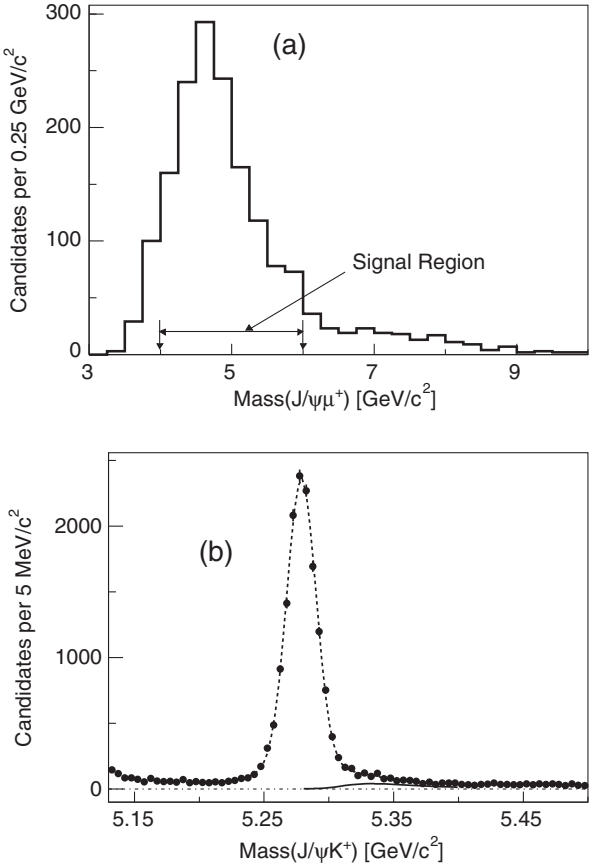

FIG. 4. (a) Distribution of invariant mass for $J/\psi\mu^+$ candidates with transverse momentum of the $J/\psi\mu^+$ system greater than 6 GeV$/c$ and (b) invariant-mass distribution of the $J/\psi K^+$ candidates for B^+ decay. The Cabibbo-suppressed $B^+ \to J/\psi\pi^+$ contribution is shown as a solid curve in (b).

a third track that satisfies the vertex requirement and mimics a muon in the CDF II detector but is a hadron. This mistaken identification can arise either because a kaon or pion decays in flight to a muon and produces a muon signature in the detector, a hadron passes through the calorimeter, or a hadron shower yields a track segment in the CMU and CMP chambers. The estimation of the misidentified-muon background directly from the data is discussed in Sec. IV B. Finally, the $b\bar{b}$ background is estimated from a parametrization of the azimuthal opening angle between the reconstructed J/ψ meson and the third muon trajectory using MC simulation. This is discussed in Sec. IV C.

A. Misidentified-J/ψ-meson background

The misidentified-J/ψ-meson background is estimated using the track pairs from the sideband regions of the $\mu^+\mu^-$ invariant-mass distribution, $M(\mu^+\mu^-)$. These dimuon pairs are required to share a common vertex with the third muon. The signal dimuon mass region is defined to be within 50 MeV/c^2 of the known value of the J/ψ-meson mass, $M_{J/\psi} = 3.0969$ GeV/c^2 [4]. The sideband regions are defined as $|(M_{J/\psi} \pm 0.150) - M(\mu^+\mu^-)| < 0.050\,\text{GeV}/c^2$. The resulting $J/\psi\mu^+$ invariant-mass distribution based on misidentified-J/ψ mesons, J/ψ_{misid}, is presented in Fig. 5. We find 11.5 ± 2.4 events within 3–4 GeV/c^2, 96.5 ± 6.9 events within the 4–6 GeV/c^2 signal region, and 25 ± 3.5 events at masses greater than 6 GeV/c^2.

B. Misidentified-muon background

The misidentified-muon background arises from real J/ψ decays that form a good three-track vertex with a hadron that is misidentified as a muon. We determine this background from the data as a function of the momentum of the third charged particle by using the J/ψ-track sample combined with knowledge of the fraction of pions, kaons, and protons in the J/ψ-track sample and the probability of each hadron type to be misidentfied as a muon. Equation (3) gives the total probability W that the third track in an event in the J/ψ-track sample is misidentified as a muon:

$$W = \epsilon_\pi(1 + F_\pi^{\text{out}})F_\pi + \epsilon_K(1 + \alpha F_K^{\text{out}})F_K + \epsilon_p F_p, \quad (3)$$

where $\epsilon_{\pi,K,p}$ are the probabilities for the relevant particle type to be misidentified as a muon, and $F_{\pi,K,p}$ are the fractions of the relevant particle types within the J/ψ-track sample. The $\epsilon_{\pi,K,p}$ are determined as functions of the p_T of the third particle, and the $F_{\pi,K,p}$ are determined as functions of the momentum of the third particle. The terms $1 + F_\pi^{\text{out}}$ and $1 + \alpha F_K^{\text{out}}$ are corrections to the probabilities for pions and kaons, respectively, to be misidentified as muons and are discussed in Sec. IV B 2. For each event in the J/ψ-track sample, reconstructed assuming that the third track is a muon, we determine W and sum these weights as functions of the $J/\psi\mu^+$ invariant mass of the events. The result is a measurement of the misidentified-muon background in the $J/\psi\mu^+$-event sample as a function of the $J/\psi\mu^+$ invariant mass. The invariant-mass distribution of the J/ψ-track system is shown in Fig. 6.

1. Probability for a p, $\pi^\pm$, or $K^\pm$ to be misidentified as a muon

The calculation of the probability for a proton to be misidentified as a muon is done using protons from reconstructed $\Lambda \to p\pi$ decays. In selecting the proton candidates we use the selection requirements for the third charged-particle from the $B_c^+ \to J/\psi\mu^+\nu$ candidates to be a muon. To determine an appropriate Λ mass range, we reconstruct the $p\pi^-$ final state for candidates with no muon match requirement. Based on the mass resolution of the $p\pi^-$ final state fit to a single Gaussian, we search in a mass range that is six standard deviations wide and centered at the known Λ mass. We find no evidence for the proton

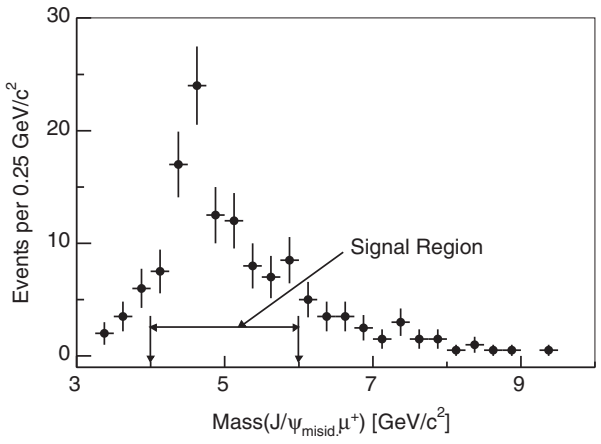

FIG. 5. Invariant-mass distribution of the $J/\psi_{\text{misid}}\mu^+$ system.

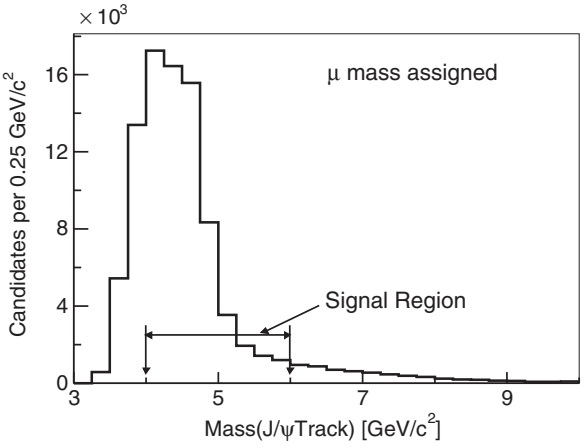

FIG. 6. Invariant-mass distribution of the J/ψ-track system. This sample is used in the misidentified-muon calculation.

punch-through process. Therefore, using the uniform distribution of the invariant mass of $p\pi^-$ pairs in the Λ mass region for a data sample with matched CMUP muons, we establish an upper limit at the 95% confidence level that ϵ_p is less than 3.4×10^{-4}. This upper limit applies to antiprotons as well.

To measure the probability for charged pions and kaons to be misidentified as muons, we use samples of well-identified pions and kaons obtained from a D^{*+} sample collected using the SVT trigger as discussed in Sec. II C. We reconstruct the decay chain $D^{*+} \to D^0(K^-\pi^+)\pi^+$. The pions and kaons are selected using the requirements listed in Table III. We also require that in a D^0 decay, the track being examined for a misidentified muon meets the same selection requirements as the third track in the J/ψ-track sample. Figure 7 shows the invariant-mass distributions of $K^-\pi^+$ pairs from D^0 decays where the hadron under test is not matched [Figs. 7(a)–(c)], and where it is matched [Figs. 7(d)–(f)] with a muon that satisfies the third-muon selection requirements. The fit function consists of a double Gaussian [Figs. 7(a)–(c)], or a single Gaussian [Figs. 7(d)–(f)], plus a second-order polynomial. Simulation shows that the enhancement in the low-mass sideband of the sample in which pions are misidentified as CMUP muons results from $D^0 \to K^-\mu^+\nu$ semileptonic decays.

We consider two options to fit the D^0 peak shown in Figs. 7(d)–(f): first, using a double-Gaussian template derived from the fit of the data sample where no matched muons are present, and second, with a single Gaussian. We choose the single-Gaussian fit because the matched sample has poor statistics and the unmatched and matched samples are not expected to have the same widths because additional broadening may occur as a result of the decay-in-flight phenomenon discussed in Sec. IV B 2. We compare the results from the double-Gaussian template with the single-Gaussian fit in order to estimate the systematic uncertainty associated with the fit model.

The muon-misidentification probability $\epsilon_{\pi^\pm,K^-,K^+}$ is given by Eq. (4),

$$\epsilon_h = \frac{N_h^{\text{with}\,\mu}}{N_h^{\text{no}\,\mu} + N_h^{\text{with}\,\mu}}, \tag{4}$$

where h is a $\pi^\pm$, K^-, or K^+; $N_h^{\text{no}\,\mu}$ represents the number of candidates where h is not matched with a CMUP muon; and $N_h^{\text{with}\,\mu}$ is the number of candidates where h is matched with a CMUP muon. The $N_h^{\text{no}\,\mu}$ values are determined by the integrals under the fitted double Gaussian within a 100 MeV/c^2 range, and the $N_h^{\text{with}\,\mu}$ are determined by the corresponding single-Gaussian integrals also within a 100 MeV/c^2 range. The muon-misidentification probabilities as functions of hadron p_T are shown in Fig. 8. The uncertainties shown are statistical only.

The muon-misidentification probabilities for K^+ hadrons are significantly higher than for K^-. The observed difference results from the different interaction cross sections for K^+ and K^- hadrons with matter, which leads to different punch-through probabilities. These effects are discussed further in Sec. IV B 2. We find no significant differences in the misidentification probabilities of π^+ and π^- mesons.

2. Corrections to $\pi^\pm$, K^-, and K^+ probabilities to be misidentified as a muon

In Eq. (3) the terms $1 + F_\pi^{\text{out}}$ and $1 + \alpha F_K^{\text{out}}$ are corrections to the probabilities for pions and kaons, respectively, to be misidentified as muons. They arise because of mass resolution effects associated with the decay in flight of pions and kaons where the decay muon is ultimately matched with a third track and results in the event contributing to the misidentified-muon background. The misidentified-muon probabilities determined above are derived under the assumption that the pion and kaon tracks, even after a possible kink resulting from a decay in flight, yield a two-body invariant mass that remains within 50 MeV/c^2 of the known D^0 mass. However, the mass resolution can be spoiled because of a kink, while the pion or kaon track is still matched to a CMUP muon. Because the signal region for $B_c^+ \to J/\psi\mu^+\nu$ decays has a width of

TABLE III. Pion and kaon particle selection requirements.

Selection requirement	Value	Comments
$q(\pi)q(\pi)$	1	Same sign
p_T of π or K	>3 GeV/c	Same as in $B_c^+ \to J/\psi\mu^+\nu$
$p_T(K^-\pi^+)$	>3 GeV/c	D^0
$\Delta\phi(K^-\pi^+)$	0.035–2.36 rad.	
Vertex χ^2 prob	>0.001	D^0 and D^{*+}
L_{xy}	>100 μm	D^0
$\lvert M(K\pi\pi) - M(K\pi) - 145.7\ \text{MeV}/c^2\rvert$	<2 MeV/c^2	$D^{*+} \to D^0\pi^+$ tagging
CMUP boundary	Inside boundary	Same as in $B_c^+ \to J/\psi\mu^+\nu$
Match with XFT	Is XFT	Same as in $B_c^+ \to J/\psi\mu^+\nu$
Isolation at CMU	No tracks <40 cm	Same as in $B_c^+ \to J/\psi\mu^+\nu$
dE/dx hits	≥ 43 hits	Same as in $B_c^+ \to J/\psi\mu^+\nu$

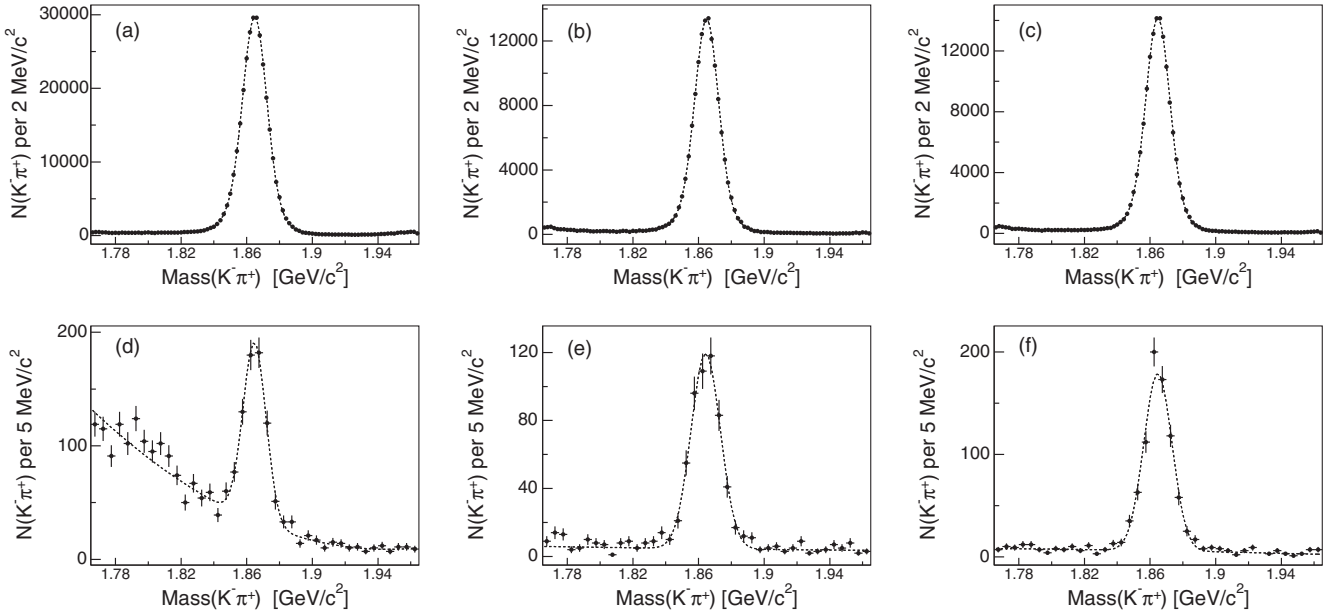

FIG. 7. Invariant-mass distributions of $K^-\pi^+$ pairs from D^0 decays where the hadron of interest is not matched (a)–(c), and where it is matched (d)–(f) with a muon that satisfies the third-muon selection requirements. Figures (a)–(f) are paired vertically with (a) and (d), (b) and (e), and (c) and (f) corresponding to $\pi^\pm$, K^-, and K^+, respectively. Examples are shown for the p_T region 3.0–3.3 GeV$/c$. The fit function consists of a double Gaussian (a)–(c), or a single Gaussian (d)–(f), plus a second-order polynomial.

2 GeV$/c^2$, background events from decays in flight may contribute to the signal region but remain excluded from the measurement of the probability that a pion or kaon is misidentified as a muon using the decay $D^0 \to K^-\pi^+$. We correct for this effect by determining the fraction $F_h^{\rm out}$ (h is a pion or kaon) of misidentified events that fall outside of the D^0 mass peak for a given particle type through a MC simulation.

The term $1 + \alpha F_K^{\rm out}$ involves an additional correction factor α that is set to 1 for K^- mesons and to $\alpha = \epsilon_{K^-}/\epsilon_{K^+}$, which is less than 1, for K^+ mesons. The rationale is as follows: Fig. 8 shows that the muon-misidentification probabilities for K^+ mesons are significantly higher than for K^- mesons. This difference arises because K^+ mesons have an additional punch-through component, which is not present for K^- mesons because the strong-interaction cross section in matter for K^- mesons is larger than that for K^+ mesons. The punch-through component does not produce any kink in the track and for this component of ϵ_{K^+} the outside-of-peak correction should not be applied. The outside-of-peak correction is needed only for the decay-in-flight fraction of ϵ_{K^+}, which is modeled as the ratio $\alpha = \epsilon_{K^-}/\epsilon_{K^+}$.

We determine the fractions $F_h^{\rm out}$ as functions of pion and kaon p_T by using simulated $D^{*+} \to D^0(\to K^-\pi^+)\pi^+$ decays selected as the corresponding control sample of data. Figure 9 shows simulated invariant-mass distributions of $K^-\pi^+$ pairs from D^0 decays for $\pi^\pm$, K^-, and K^+ mesons passing the selection requirements for a CMUP muon (see Sec. II B). Example distributions are given for the p_T range 3.0–3.3 GeV$/c$.

The simulated data shown in Fig. 9 are fit with a single Gaussian plus a second-order polynomial. The fraction of the muon misidentifications outside of the D^0 mass peak for each p_T interval is calculated as follows:

$$F_h^{\rm out} = \frac{N_h - N_h^{\rm peak}}{N_h^{\rm peak}}, \tag{5}$$

where N_h represents, in each p_T bin of the relevant final-state hadron h, the number of events that pass the

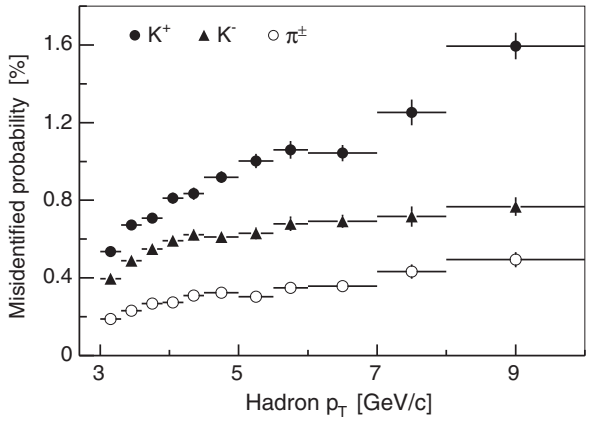

FIG. 8. Muon-misidentification probabilities for K^+, K^-, and $\pi^\pm$ as functions of hadron p_T.

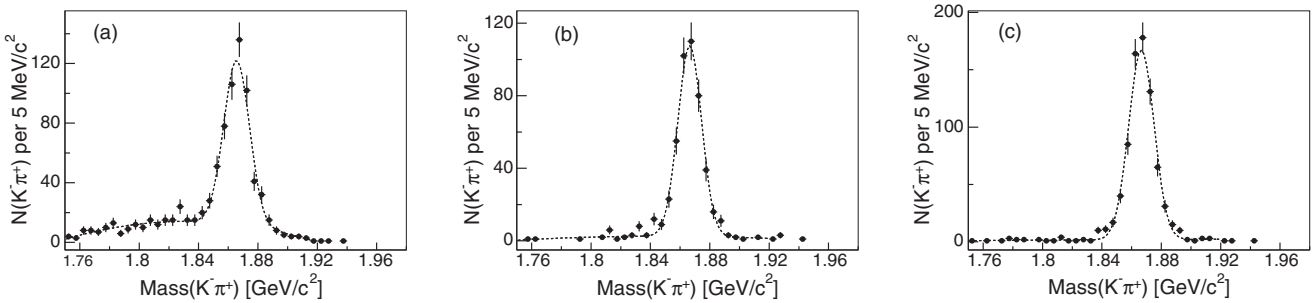

FIG. 9. Invariant-mass distributions of $K^-\pi^+$ pairs from simulated $D^0 \to K^-\pi^+$ decays for (a) $\pi^{\pm}$, (b) K^-, and (c) K^+ mesons passing the selection requirements for a CMUP muon. Example distributions are given for the p_T range 3.0–3.3 GeV/c. The fit function consists of a single Gaussian plus a second-order polynomial.

requirements for h to match a CMUP muon and N_h^{peak} represents the integral under the single-Gaussian component of the fit to the distribution within 50 MeV/c^2 of the peak of the Gaussian. In order to estimate the systematic uncertainty, we fit the above distributions with width values derived from the experimental data analyzed in Sec. IV B 1.

Figure 10 shows the fraction of events with a CMUP muon whose $K\pi$ invariant mass falls outside of the D^0 mass peak due to decay in flight for $\pi^{\pm}$, K^-, and K^+ mesons from the $D^{*+} \to D^0(K^-\pi^+)\pi^+$ decay chain as a function of hadron p_T.

3. Hadron fractions within the J/ψ-track sample

The proton, pion, and kaon fractions in the J/ψ-track sample comprise the other essential component required to complete the data-driven calculation of the misidentified-muon background.

The pion fraction F_π of the tracks in the J/ψ-track sample as a function of particle momentum is determined using dE/dx measured in the COT. The remaining fraction F_{K+p} of tracks in the J/ψ-track sample is a combination of kaons and protons because the kaon and proton dE/dx distributions in the COT are indistinguishable at momentum greater than 3 GeV/c. The proton fraction F_p is measured within the 2.0–3.3 GeV/c momentum range using a simultaneous fit of the dE/dx and time-of-flight data. Also available is the predicted F_p from MC simulation for momenta greater than 3.0 GeV/c. Using the two fractions F_p in the 3.0–3.3 GeV/c momentum range, one from the experimental data and a second from simulation, F_p from simulation is scaled to agree with the experimental data in the momentum range 3.0–3.3 GeV/c. Thus, F_p is taken from the scaled simulation for particle momentum greater than 3.0 GeV/c. Then the kaon particle fraction F_K in the J/ψ-track sample for particle momentum greater than 3.0 GeV/c is given by $1 - F_\pi - F_p$.

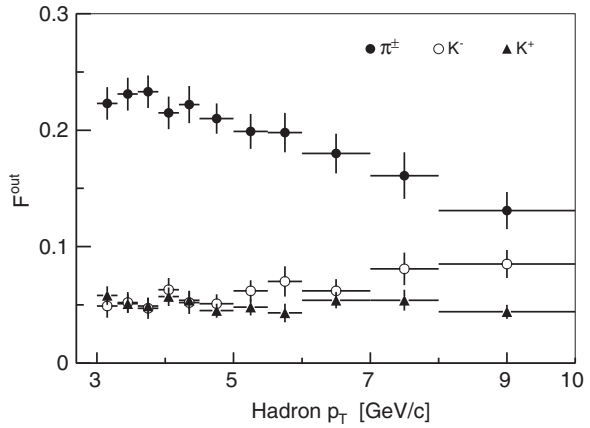

FIG. 10. Fraction of events with a CMUP muon whose $K\pi$ invariant mass falls outside of the D^0 mass peak due to decay in flight: • for the $F^{\text{out}}_{\pi^{\pm}}$, ∘ for the $F^{\text{out}}_{K^-}$, and ▲ for the $F^{\text{out}}_{K^+}$, respectively.

To estimate the F_π and F_{K+p} fractions, we use the dE/dx information contained in the separation-significance quantity $\mathcal{S}$,

$$\mathcal{S} = \frac{dE/dx_{\text{meas}} - dE/dx_\pi}{\sigma_{dE/dx}}, \tag{6}$$

where dE/dx_{meas} is the measured energy loss for a given third track from the J/ψ-track sample, dE/dx_π is the predicted energy loss for the π hypothesis, and $\sigma_{dE/dx}$ is the estimated uncertainty of the measurement. In this analysis the third track in the J/ψ-track sample has contributions not only from pions, but also kaons and protons. The predicted mean value is about -1.5 for kaons and protons and about zero for pions. Because the $\mathcal{S}$ distribution for each component is asymmetric, we model it empirically with the sum of two gamma distributions and use the results from a simpler Gaussian fit to evaluate the systematic uncertainty associated with the fit model. The probability density written in terms of $\mathcal{S}$ is defined by

$$G(\gamma, \beta, \mu; \mathcal{S}) = \frac{(\frac{\mathcal{S}-\mu}{\beta})^{\gamma-1} \exp(-(\frac{\mathcal{S}-\mu}{\beta}))}{\beta\Gamma(\gamma)} \tag{7}$$

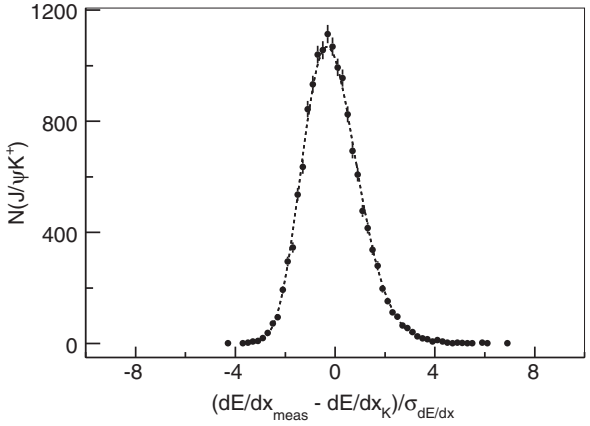

FIG. 11. Distribution of $\mathcal{S}$ from Eq. (6) for the K hypothesis using the K^+ tracks from the $B^+ \to J/\psi K^+$ decays [see Fig. 4(b)]. The distribution is fit with a gamma function, where all three parameters (γ, β, and μ) are allowed to float.

for $\mathcal{S} > \mu$ and zero otherwise where Γ is the Euler gamma function. The distribution has a mean $\gamma\beta + \mu$ and variance $\gamma\beta^2$. In the limit of large γ this asymmetric distribution approaches a Gaussian distribution. The parameters γ and β are positive real numbers that control the shape, mean, and variance of the distribution, and μ is the location parameter.

In order to find parameters to use for the kaon gamma distribution and gain guidance for pions, we use kaons from the $B^+ \to J/\psi K^+$ decays [see Fig. 4(b)]. The kaon tracks are identified by requiring the $J/\psi K^+$ mass to be within 40 MeV/c^2 (approximately 3σ) of the known B^+ mass [4]. Figure 11 shows the distribution of a quantity similar to $\mathcal{S}$ from Eq. (6), but where the kaon hypothesis for the predicted energy loss dE/dx_K is used. Figure 11 illustrates that the dE/dx distribution for kaons is not Gaussian. A least-squares fit returns the following values: $\gamma = 23.5 \pm 2.5$, $\beta = 0.230 \pm 0.013$, and $\mu = -5.49 \pm 0.28$. Using these parameters we calculate the width $\sigma = \beta\sqrt{\gamma} = 1.11 \pm 0.13$ and mean $\gamma\beta + \mu = -0.09 \pm 0.01$. A value of 23 for the γ parameter models accurately the kaons across their full momentum spectrum and is used for the fit of the $K + p$ fraction in the J/ψ-track sample. For the width σ, we choose a higher value of 1.15 to take into account the contributions from protons. As a fit function for the pions we also use the gamma distribution. Finally, the dE/dx data are fit with the following formula:

$$N_{\rm ev}(\mathcal{S}) = N_{\rm fit}[F_\pi G(\gamma_\pi, \beta_\pi, \mu_\pi; \mathcal{S}) + (1 - F_\pi) \times G(\gamma_{K+p}, \beta_{K+p}, \mu_{K+p}; \mathcal{S})], \quad (8)$$

where $N_{\rm ev}(\mathcal{S})$ is the prediction as a function of the quantity in Eq. (6), $N_{\rm fit}$ is the number of events, F_π is the pion fraction, and G is the probability density function of the gamma distribution. There are only two free parameters in this least-squares fit: $N_{\rm fit}$ and F_π. The parameter μ_{K+p} is adjusted as a function of pion and kaon momentum because the $K + p$ dE/dx distribution changes slowly with respect to that of the pion as the particle momentum changes.

Figure 12 shows the distributions of $\mathcal{S}$ for the positively charged third tracks in three momentum ranges fit with a sum of two gamma distributions as described in Eq. (8).

To calculate the proton fraction, we first calibrate the ToF performance using the kaon tracks from $B^+ \to J/\psi K^+$ decays in the momentum range 2.0–3.3 GeV/c. Then we perform a simultaneous two-dimensional likelihood fit of the ToF and the dE/dx data for the third track in the J/ψ-track sample. As an example of the ToF standalone information, Fig. 13 shows the distribution of the quantity $\frac{\mathrm{ToF_{meas}} - \mathrm{ToF}_\pi}{\sigma_{\rm ToF}}$ using the momentum range 2.0–2.2 GeV/c for events restricted to the subset with $-1.7 < \mathcal{S} < -1.5$. Here, $\mathrm{ToF_{meas}}$ is the measured time, ToF_π is the predicted time for the pion hypothesis, and $\sigma_{\rm ToF}$ is the uncertainty in the measured time.

To make use of the determination of F_p in the momentum range 2.0–3.3 GeV/c, we simulate F_p for momentum in the range greater than 3.0 GeV/c. The MC procedure generates realistic $b\bar{b}$ quark events using the PYTHIA [28] simulation package with all $2 \to 2$ QCD processes and initial- and final-state radiation. The CTEQ5L [29] parton distributions for protons are used, and fragmentation of the b quarks employs the Lund string model [30,31].

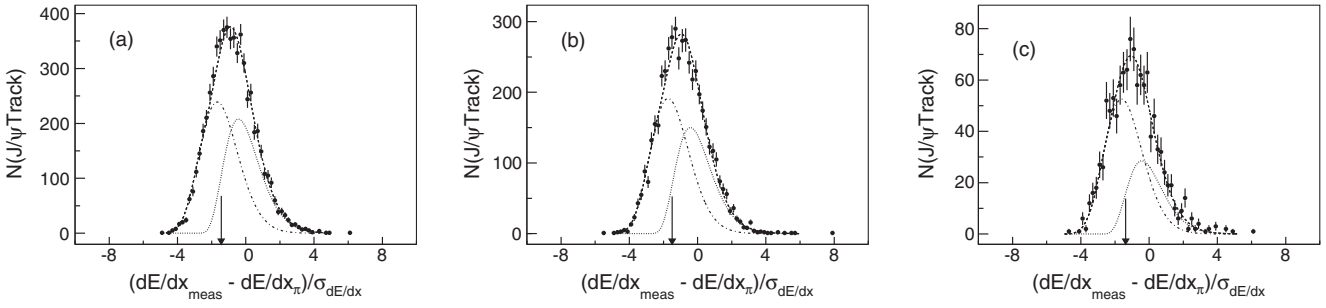

FIG. 12. Distributions of $\mathcal{S}$ for the positively charged third tracks in three momentum ranges: (a) 3.0–3.3 GeV/c, (b) 4.2–4.5 GeV/c, and (c) 6.0–7.0 GeV/c. The fit function consists of the sum of two gamma distributions, one for pions (dotted curve), and a second one for $K + p$ (dash-dot curve). The total fit function is shown as a dashed curve. Details of the fit are discussed in the text.

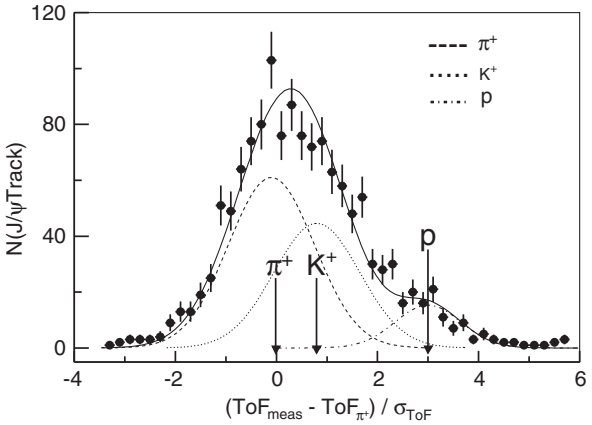

FIG. 13. Distribution of the quantity $\frac{\mathrm{ToF}_{\mathrm{meas}}-\mathrm{ToF}_{\pi}}{\sigma_{\mathrm{ToF}}}$ using the momentum range 2.0–2.2 GeV/c for the events restricted to the subset with $-1.7 < \mathcal{S} < -1.5$. Arrows show the central positions of the π, K, and p hadrons.

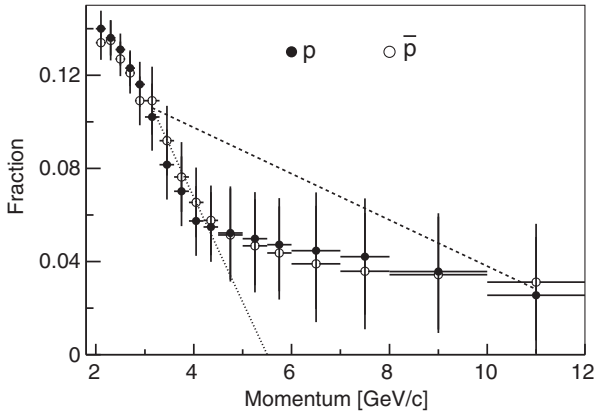

FIG. 14. Third-track p and $\bar{p}$ fractions in the J/ψ-track sample. The systematic uncertainty for the simulation prediction is bounded from above and below using the dashed and dotted lines in the figure.

The decay of B mesons and baryons utilizes EVTGEN and the CDF II detector simulation is based on GEANT3 [32]. Studies show that the PYTHIA simulation predictions are lower than the experimental measurements in the momentum range 3.0–3.3 GeV/c. To achieve consistency between the simulation and the experimental data, we scale the PYTHIA predictions for the whole range of momenta greater than 3 GeV/c so that the simulation and the experimental measurement of F_p agree in the momentum range 3.0–3.3 GeV/c. Both the experimental measurements for the p and $\bar{p}$ fractions in the momentum range 2.0–3.3 GeV/c and the scaled PYTHIA predictions in the range of momenta greater than 3 GeV/c are shown in Fig. 14.

For the study of the systematic uncertainty in the proton fractions we consider two options. The first is to follow the slope of the simulation in the region 3.0–4.2 GeV/c assuming that $F_p = 0$ at momenta higher than 5.5 GeV/c, and the second is to assume a straight line connecting the lowest and highest momentum points in the simulation (see the dotted and dashed lines in Fig. 14).

Using the combined fraction F_{K+p}, determined from the fit illustrated in Fig. 12, and the standalone fraction F_p illustrated in Fig. 14, the fraction F_K is determined. Figure 15 shows the F_π, F_K, and F_p fractions for the (a) positively and (b) negatively charged particles with momenta greater than 3 GeV/c corresponding to the third tracks in the J/ψ-track system.

4. Results and systematic uncertainties for the misidentified-muon background

To complete the misidentified-muon background calculation, for each third track in the J/ψ-track sample, we assign a weight W according to Eq. (3) using the kaon and pion misidentification probabilities shown in Fig. 8; the fraction of the muon events outside of the D^0 mass peak shown in Fig. 10; and the pion, kaon, and proton fractions shown in Fig. 15. The weighted mass distribution corresponds to the distribution of the misidentified-muon background as a function of the $J/\psi\mu^+$ invariant mass.

An additional small misidentified-muon component is produced if a misidentified J/ψ makes a three-track vertex with a misidentified muon ("doubly misidentified"). Since this background is in both the misidentified-J/ψ and the misidentified-muon backgrounds, it must be determined to avoid double counting it. The doubly misidentified correction is calculated using the invariant-mass distribution of the sideband dimuons in the J/ψ_{side}-track system following procedures the same as those discussed in this section of the paper.

Because of the large size of the J/ψ-track sample, the statistical uncertainties in the calculation of the misidentified-muon background are negligible compared with the systematic uncertainties. For the misidentified-muon uncertainties, the following procedures are used to estimate the various components of the systematic uncertainty:

(1) For the muon-misidentification probabilities of pions or kaons, a comparison is made of results from two fit functions applied to the same distributions associated with a CMUP muon: the single-Gaussian function versus the double-Gaussian templates derived from the nonmuon sample.
(2) For the fraction of the muon-matched events outside of the D^0 mass peak, fits to simulated mass distributions based on single-Gaussian functions with widths fixed to those observed in data are compared with fits in which widths are free to float. The resulting differences are used to estimate the systematic uncertainty for this part of the misidentified-muon calculation.
(3) For the particle fractions in the J/ψ-track system, fits of the dE/dx data with a sum of two Gaussian

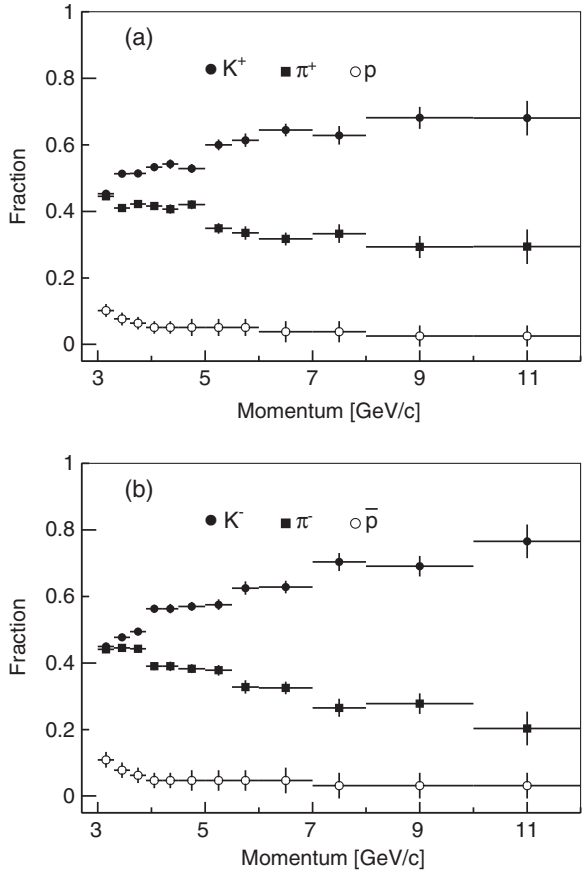

FIG. 15. Fractions F_π, F_K, and F_p for (a) positively and (b) negatively charged particles with momenta greater than 3 GeV/c corresponding to the third tracks in the J/ψ-track system.

distributions are compared to the fits with the sum of two gamma distributions to determine the systematic uncertainty in the fitting procedure.

(4) For the proton fractions, variation bounds are obtained from the data-normalized PYTHIA simulation. For the lower bound we follow the slope of the PYTHIA simulation in the region 3.0–4.2 GeV/c assuming that $F_p = 0$ beyond 5.5 GeV/c (Fig. 14, dotted line). For the upper bound we assume a straight line connecting the lowest and highest momentum points in the PYTHIA simulation (see the dashed line in Fig. 14).

The systematic uncertainties for the misidentified and doubly misidentified-muon backgrounds are shown in Table IV. The misidentified and doubly misidentified-muon backgrounds as functions of the invariant mass of the J/ψ-track system and their associated systematic uncertainties are shown in Fig. 16. Numerical results are given in Table V.

C. $b\bar{b}$ background

The $b\bar{b}$ background arises from the combination of a J/ψ meson produced by the decay of a b quark with the third muon produced from the decay of the $\bar{b}$ quark in the same event, or vice versa. The production of $b\bar{b}$ pairs in $p\bar{p}$ collisions is dominated by the leading-order flavor-creation (FC) process and the next-to-leading-order flavor-excitation (FE) and gluon-splitting (GS) processes [33]. Flavor creation corresponds to the production of a $b\bar{b}$ pair by gluon fusion or by the annihilation of light quarks via two 2-to-2 parton subprocesses $gg \to b\bar{b}$ and $q\bar{q} \to b\bar{b}$. Flavor excitation refers to the QCD hard 2-to-2 reaction corresponding to the scattering of a b quark out of the initial state into the final state by a gluon or a light quark or light antiquark via the subprocesses $gb \to gb$, $qb \to qb$, and $\bar{q}b \to \bar{q}b$. The $\bar{b}$ partner from the original initial state $b\bar{b}$ pair will also appear in the final state. There are three more processes corresponding to the scattering of the $\bar{b}$ quarks in the high Q^2 sea of gluons and heavy-quark pairs that define the p and $\bar{p}$ structure functions. Gluon splitting occurs when only gluons and light quarks and light antiquarks participate in the 2-to-2 hard parton scattering subprocess, but one of the final-state gluons fragments into a $b\bar{b}$ pair,

TABLE IV. Systematic uncertainties in the number of events involving misidentified muons and doubly misidentified muons.

Source	Misidentified	Doubly misidentified
Misidentification probability	±7.3	±0.4
Fraction of events outside of the D^0 mass peak	±1.2	±0.1
Particle fractions in the J/ψ-track system	±4.7	±0.3
Proton fractions	$^{+4.0}_{-14.0}$	$^{+0.2}_{-0.7}$
Total	$^{+9.6}_{-16.5}$	$^{+0.5}_{-0.9}$

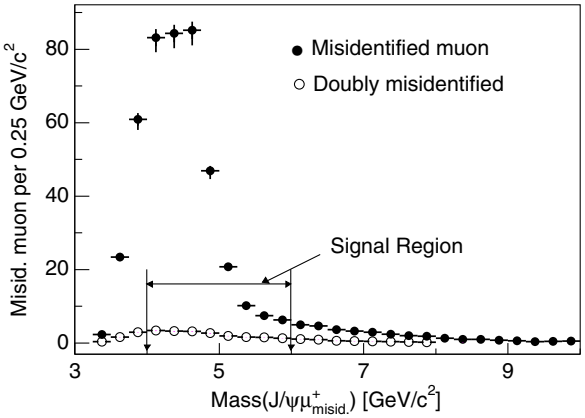

FIG. 16. Weighted invariant-mass distribution of the J/ψ-track system showing the misidentified (filled circles) and the doubly misidentified (open circles) muon backgrounds to the $B_c^+ \to J/\psi\mu^+X$ decays. The error bars represent the estimated systematic uncertainties. Because of the large size of the J/ψ-track sample, the statistical errors in the misidentified-muon calculation are negligible.

TABLE V. Number of events involving misidentified-muon and doubly misidentified-muon backgrounds within the signal and sideband mass ranges and associated systematic uncertainties.

Mass range (GeV/c^2)	3–4	4–6	>6
Misidentified muons	$86.7^{+2.4}_{-4.2}$	$344.4^{+9.6}_{-16.5}$	$32.1^{+0.9}_{-1.5}$
Doubly misidentified muons	$5.1^{+0.1}_{-0.2}$	$19.0^{+0.5}_{-0.9}$	$5.2^{+0.1}_{-0.3}$

e.g., $gg \to g(g \to b\bar{b})$ or $qg \to q(g \to b\bar{b})$. Flavor creation is expected to produce the largest opening angles between the quark pairs, as measured in the plane transverse to the beam direction. Flavor excitation is expected to produce both large and small opening angles, and gluon splitting is expected to produce a relatively uniform distribution of opening angles [28,29].

The determination of the $b\bar{b}$ background relies on a PYTHIA MC simulation to generate potential $b\bar{b}$ background events for the three QCD processes. We constrain the PYTHIA MC simulation with the experimental data using the distribution of the opening angle $\Delta\phi$ between the J/ψ and the muon in an event. We select a sample of experimental data called the unvertexed-$J/\psi\mu^+$-pairs sample as described in Sec. IV C 1 below. Unvertexed means that there are no requirements that the $J/\psi\mu^+$ pairs originate from a common vertex. From this sample we subtract potential signal candidates as well as unvertexed variations of the major backgrounds described above. We fit the $\Delta\phi$ distribution in these data with a linear combination of the $\Delta\phi$ distributions of PYTHIA-simulated FC, FE, and GS events that are also unvertexed. This procedure allows for a determination of the relative fractions of FC, FE, and GS to use in estimating the $b\bar{b}$ background irrespective of the relative fractions that any particular variation of the PYTHIA parameters might produce. Using the experimentally constrained fractions for the FC, FE, and GS contributions, we calculate the $b\bar{b}$ background by applying the selection requirements for the $J/\psi\mu^+$-signal sample to the unselected PYTHIA-simulated FC, FE, and GS samples. A valuable cross-check of the background determination consists in comparing the sum of all of the backgrounds with the number of events in the $J/\psi\mu^+$ invariant-mass ranges 3–4 GeV/c^2 and greater than 6 GeV/c^2, where the number of events is dominated by background.

1. Selecting the unvertexed-$J/\psi\mu^+$ pairs

The selection requirements for the unvertexed-$J/\psi\mu^+$-pairs sample in the data follow the requirements listed in Tables I–II with the modifications: the mass range for the J/ψ is reduced from ± 50 MeV/c^2 to ± 30 MeV/c^2; the decay length for the J/ψ is required to be greater than 200 μm; there is no vertex requirement for the trimuon system; and there is no $\Delta\phi$ requirement between the J/ψ and the third muon. In the data there may be more than one $p\bar{p}$ interaction distributed longitudinally along the interaction region, which has a rms length of about 30 cm. In order to restrict the data sample to events in which the J/ψ and third muon come from the same $p\bar{p}$ interaction, we require that the z separation between the J/ψ and the third muon is less than 2 cm.

The unvertexed-$J/\psi\mu^+$ pairs come not only from different b hadrons produced in the same $p\bar{p}$ interaction but also from non-$b\bar{b}$ sources:

(1) Single b hadrons contribute to the unvertexed-$J/\psi\mu^+$ pairs that would pass the vertex probability requirement. They include the $B_c^+ \to J/\psi\mu^+X$ event candidates which include the background components having a vertexed J/ψ plus a misidentified muon and misidentified vertexed J/ψ plus a muon.
(2) A pion or kaon from an unvertexed J/ψ-track event is misidentified as a muon.
(3) An unvertexed misidentified J/ψ also can be in the unvertexed-$J/\psi\mu^+$ system.

To produce a pure sample of $b\bar{b}$ pairs to compare with the PYTHIA simulation, it is necessary to estimate the contributions from the non-$b\bar{b}$ sources listed above and then subtract them from the selected sample of unvertexed-$J/\psi\mu^+$ pairs shown in Fig. 17(a). The first non-$b\bar{b}$ source is identified by applying the vertex probability requirement to the unvertexed-$J/\psi\mu^+$ pairs, and its $\Delta\phi$ distribution is shown in Fig. 17(b), labeled as "$B_c^+ \to J/\psi\mu^+\nu$"

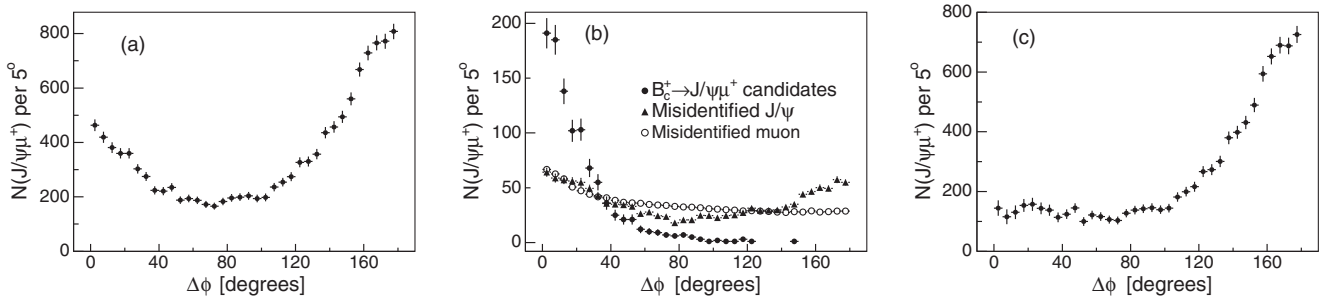

FIG. 17. (a) Distribution versus $\Delta\phi$ of all unvertexed-$J/\psi\mu^+$ pairs from the experimental data. (b) Three non-$b\bar{b}$ contributions to (a) superimposed. (c) Experimental data from (a) with the non $b\bar{b}$ contributions removed.

candidates. The essential difference between this $B_c^+ \to J/\psi\mu^+\nu$ sample and the signal sample is that the $\Delta\phi$ selection criterion is not applied in order to compare the $b\bar{b}$ data sample with the MC simulation over the entire range $\Delta\phi$. Next, we estimate the unvertexed misidentified-muon background with the procedure described in Sec. IV B using the unvertexed-J/ψ-track sample with the vertexed events subtracted. The $\Delta\phi$ distribution of unvertexed misidentified-muon background is also shown in Fig. 17(b). Finally, the events containing an unvertexed-$J/\psi\mu^+$ pair, where the J/ψ is misidentified, are accounted by the method of Sec. IV A using the events from the dimuon mass sidebands of the unvertexed-$J/\psi\mu^+$-pairs sample. The $\Delta\phi$ distribution of misidentified J/ψ in the unvertexed-$J/\psi\mu^+$-pairs sample is also shown in Fig. 17(b). Subtracting the three non-$b\bar{b}$ sources shown in Fig. 17(b) from the unvertexed-$J/\psi\mu^+$ pairs in Fig. 17(a) gives the background-subtracted sample of unvertexed-$J/\psi\mu^+$ pairs. This pure $b\bar{b}$ sample is shown in Fig. 17(c) and is used to determine the relative fractions of the QCD production processes generated by the PYTHIA simulations.

2. Simulated unvertexed-$J/\psi\mu^+$ pairs

A PYTHIA sample containing 0.5×10^6 $b\bar{b}$ pairs is generated. Either the b or $\bar{b}$ quark is allowed to decay naturally, where the major sources of muons are semileptonic decays of bottom hadrons or of their daughter charm hadrons. The $\bar{b}$ or b quark partner is forced to decay into a J/ψ or any state which might cascade into a J/ψ meson. Figures 18(a)–(c) show the $\Delta\phi$ distributions of unvertexed-$J/\psi\mu^+$ pairs from the FC, FE, and GS processes, respectively.

To normalize the $b\bar{b}$ background events from the PYTHIA sample to data, we use the yields of the $B^+ \to J/\psi K^+$ decays observed in data. In the $B^+ \to J/\psi K^+$ decays reconstructed from the PYTHIA simulation we apply all the requirements listed in Tables I–II. The numbers of $B^+ \to J/\psi K^+$ decays produced by the three QCD processes are $16\,275 \pm 130$ (25% of FC), $35\,464 \pm 189$ (55% of FE), and $12\,602 \pm 118$ (20% of GS).

3. Fitting the unvertexed-$J/\psi\mu^+$ $\Delta\phi$ distribution

The experimental data shown in Fig. 17(c) are fit with a linear combination of the three PYTHIA $\Delta\phi$ distributions shown in Figs. 18(a)–(c). The predicted number of $b\bar{b}$ events for a given $\Delta\phi$ bin is given by

$$N_{b\bar{b}} = C(S_{FC}N_{b\bar{b}}^{FC} + S_{FE}N_{b\bar{b}}^{FE} + S_{GS}N_{b\bar{b}}^{GS}) \times \frac{N_{B^+}}{S_{FC}N_{B^+}^{FC} + S_{FE}N_{B^+}^{FE} + S_{GS}N_{B^+}^{GS}}. \quad (9)$$

$C = 0.76 \pm 0.07$ is a correction factor that accounts for the differences between the fraction of b quarks fragmenting into B^+, the $B^+ \to J/\psi K^+$ branching fraction, and the known inclusive branching fraction for all B hadrons to produce a J/ψ meson [4] and the values set in the PYTHIA simulation program [28]. In the fit C is constrained by its uncertainty. The parameters S_{FC}, S_{FE}, and S_{GS} are the scale factors for the different QCD production processes in PYTHIA. The fit allows the scale factors to float subject to the constraint that their sum must equal three. The numbers of PYTHIA events in a given $\Delta\phi$ bin as shown in Figs. 18(a)–(c) are $N_{b\bar{b}}^{FC}$, $N_{b\bar{b}}^{FE}$, and $N_{b\bar{b}}^{GS}$, respectively. The total number of $B^+ \to J/\psi K^+$ decays in the data shown in Fig. 4(b) is N_{B^+}. The numbers of $B^+ \to J/\psi K^+$ decays produced by the three QCD processes in PYTHIA are $N_{B^+}^{FC}$, $N_{B^+}^{FE}$, and $N_{B^+}^{GS}$, respectively. The last term in Eq. (9) along with C normalizes the three PYTHIA samples to the experimental data.

The result of the fit is given in Table VI. The least-squares fit disfavors a contribution from the FE process by returning S_{FE} of -0.11 ± 0.10. A linear combination of FC and GS terms gives a reasonable least-squares fit to the data. The fitting function for the FC plus GS combination is shown in Eq. (10),

$$N_{b\bar{b}} = C(S_{FC}N_{b\bar{b}}^{FC} + S_{GS}N_{b\bar{b}}^{GS}) \times \frac{N_{B^+}}{S_{FC}N_{B^+}^{FC} + S_{GS}N_{B^+}^{GS}}, \quad (10)$$

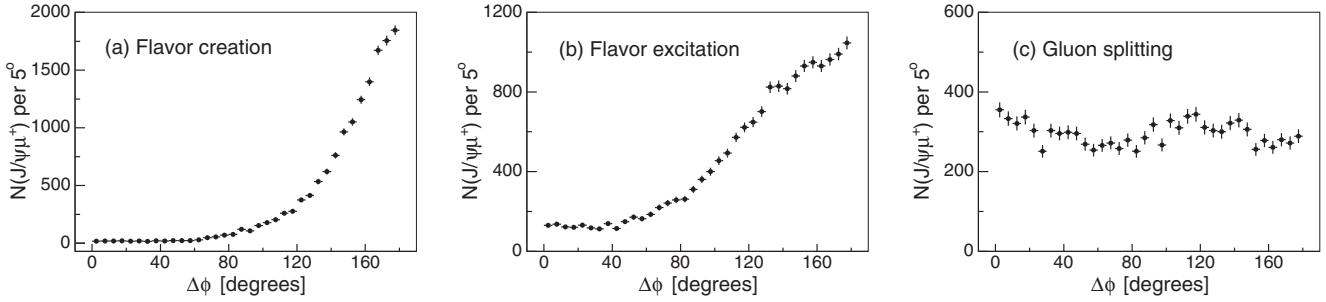

FIG. 18. Distributions of $\Delta\phi$ for the unvertexed-$J/\psi\mu^+$ pairs simulated from the three QCD production processes: (a) flavor creation, (b) flavor excitation, and (c) gluon splitting.

TABLE VI. Results of the least-squares fit of the $\Delta\phi$ distribution of the unvertexed-$J/\psi\mu^+$ data with the three QCD production processes.

	FC + FE + GS
C	0.70 ± 0.03
S_{FC}	$3\text{-}S_{FE} - S_{GS}$
S_{FE}	-0.11 ± 0.10
S_{GS}	1.60 ± 0.07
χ^2/ndf	38.5/33

where the sum of $S_{FC} + S_{GS} = 2$. Numerical results from the fit shown in Fig. 19 are as follows: $C = 0.73 \pm 0.01$, $S_{GS} = 1.02 \pm 0.03$, $S_{FC} = 2 - S_{GS}$. The factors S_{FC}, S_{GS}, and C together with Eq. (10) are used in Sec. IV C 4 to calculate the number of $b\bar{b}$ background events.

One source of systematic uncertainty in the determination of the $b\bar{b}$ background arises from the choice to force the contribution of FE to be zero. We estimate the corresponding systematic uncertainty using the difference between the predicted number of $b\bar{b}$ events for the two values 0 and 0.1 for S_{FE}. A second source is introduced by the uncertainty in the estimate of the unvertexed misidentified-muon component of the $\Delta\phi$ distribution of unvertexed-$J/\psi\mu^+$ events. The misidentified-muon component is removed prior to fitting the PYTHIA predictions to the data; hence, its uncertainty propagates into the determination of the $b\bar{b}$ background. To determine this systematic uncertainty, the $\Delta\phi$ distribution of unvertexed-$J/\psi\mu^+$ pairs shown in Fig. 17(c) is increased and decreased by the amount of the lower and upper values of the unvertexed misidentified-muon systematic uncertainty, respectively. The scale factors are refit for these two cases and the change in the predicted $b\bar{b}$ background is determined. The systematic uncertainties from these two sources are summarized in Table VII. The total systematic uncertainty is calculated by adding the results from the three rows in quadrature.

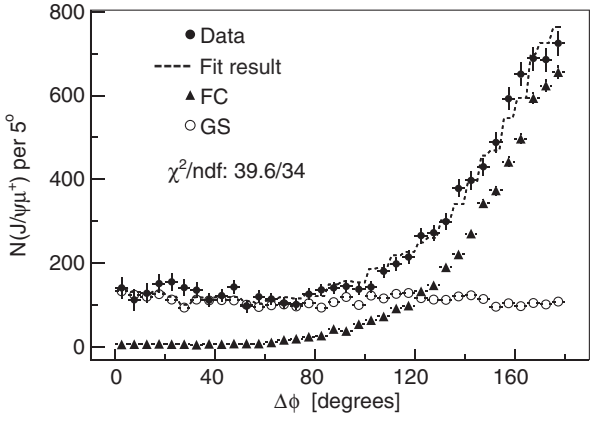

FIG. 19. Fit of the $\Delta\phi$ distribution of the unvertexed-$J/\psi\mu^+$ data for the combination of FC plus GS.

TABLE VII. Systematic uncertainties in the number of $b\bar{b}$ background events in the $J/\psi\mu^+$ mass ranges 3–4 GeV/c^2, 4–6 GeV/c^2, and greater than 6 GeV/c.

$b\bar{b}$ sys	3–4 GeV/c^2	4–6 GeV/c^2	>6 GeV/c^2
$S_{FE} = 0.0$ or 0.1	−0.3	−4.9	−3.0
Misidentified muon increased	−0.1	−1.5	−0.9
Misidentified muon reduced	+0.2	+2.7	+1.7
Total	±0.4	±5.8	±3.6

4. Results for the $b\bar{b}$ background

Having determined the correct scale factors to use for the PYTHIA simulation of the QCD $b\bar{b}$ processes, the $b\bar{b}$ background in the $J/\psi\mu^+$ event sample is calculated using Eq. (10). The number of FC and GS events from the PYTHIA simulation is determined by requiring that all the simulated $J/\psi\mu^+$ events satisfy *all* the requirements listed in Tables I–II to reconstruct the $B_c^+ \to J/\psi\mu^+\nu$ decay. In addition to the B_c^+ selection requirements for the PYTHIA sample, we require that the third muon does not originate from a pion or kaon and that it originates from a different particle than the J/ψ originates from. Other than the $J/\psi\mu^+$ events, the quantities needed for the calculation are the QCD scale factors and C, the number of B^+ mesons in the data shown in Fig. 4(b), and the numbers of $B^+ \to J/\psi K^+$ decays produced by the QCD processes in the PYTHIA simulation given in Sec. IV C 2. A summary of the input quantities and the results for the $b\bar{b}$ background in the signal region is given in Table VIII. The second column gives the numbers of $J/\psi\mu^+$ events simulated by PYTHIA passing the B_c^+ selection requirements after contributions from the dimuon sideband region are subtracted. The uncertainty in the $b\bar{b}$ background is due to several sources. There are statistical uncertainties in the yields of the four simulated samples $N_{b\bar{b}}^{FC}$, $N_{b\bar{b}}^{GS}$, $N_{B^+}^{FC}$, and $N_{B^+}^{GS}$, and in the determination of the $B^+ \to J/\psi K^+$ sample in the experimental data. Finally, there are correlated uncertainties in the parameters C, S_{FC}, and S_{GS} that are determined by the

TABLE VIII. Expected numbers of $b\bar{b}$ background events in the signal region. The uncertainties are statistical only and their sources include the sizes of the trimuon systems, the number of B^+ events, and the statistical uncertainty of the scale factors. The value of C returned by the fit is 0.73 ± 0.01, while the expected one is 0.76 ± 0.07.

$b\bar{b}$ background	$N_{b\bar{b}}$(MC)	S_i	N_{B^+}(MC)	$N_{b\bar{b}}$
FC	36.5	$2 - S_{GS}$	16275 ± 130	12.9 ± 4.1
FE	185	0	35464 ± 189	0
GS	443.5	1.02 ± 0.03	12602 ± 118	165.7 ± 11.7
Total		-	-	178.6 ± 12.4

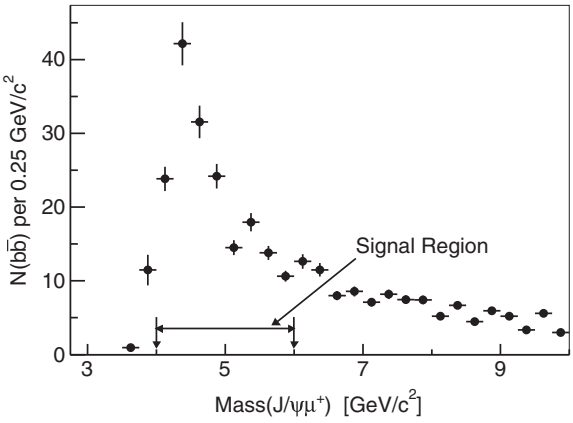

FIG. 20. Invariant-mass distribution of the $b\bar{b}$ background determined from a PYTHIA MC simulation constrained by the experimental data. The error bars represent the statistical uncertainties.

fit to the $\Delta\phi$ distribution in the unvertexed-$J/\psi\mu^+$ sample. The resulting invariant-mass distribution of the $b\bar{b}$ background is shown in Fig. 20.

The total $b\bar{b}$ background event yields in the invariant-mass ranges 3–4 GeV/c^2, 4–6 GeV/c^2, and greater than 6 GeV/c^2 are $12.4 \pm 2.4(\text{stat}) \pm 0.4(\text{syst})$, $178.6 \pm 12.4(\text{stat}) \pm 5.8(\text{syst})$, and $110.4 \pm 10.7(\text{stat}) \pm 3.6(\text{syst})$, respectively.

D. Total background

The backgrounds to the $B_c^+ \to J/\psi\mu^+X$ decays discussed above are summarized in Table IX with their statistical and systematic uncertainties. The misidentified-J/ψ background, misidentified-muon background, and $b\bar{b}$ background are included. The doubly misidentified background contribution is subtracted to avoid double counting. Entries with no statistical uncertainties listed represent determinations for which the statistical uncertainty is negligible compared with the systematic uncertainty. The misidentified-J/ψ background is calculated using the dimuon sidebands near the J/ψ invariant mass. Since there are no systematic uncertainties that are significant, the uncertainty is only statistical.

The number N_{obs} of $B_c^+ \to J/\psi\mu^+X$ signal candidates is presented in Table X. The statistical and systematic uncertainties are combined in quadrature. The top row in Table X reports the number of reconstructed $B_c^+ \to J/\psi\mu^+X$ candidates shown in Fig. 4(a). The quantity N_{obs} is used to calculate the final $B_c^+ \to J/\psi\mu^+\nu$ yield.

V. CONTRIBUTIONS TO $B_c^+ \to J/\psi\mu^+X$ FROM OTHER B_c^+ DECAYS

After subtracting backgrounds, the trimuon sample still contains contributions from other B_c^+ decay modes, in addition to the decay $B_c^+ \to J/\psi\mu^+\nu$. For example, a B_c^+ might decay into a $\psi(2S)\mu^+\nu$ state, followed by the $\psi(2S)$ decay into a $J/\psi\pi^+\pi^-$ final state. Another example is a B_c^+ decay into $J/\psi\tau^+\nu$ state followed by the τ decay into a muon and two neutrinos. The fraction of these events that meets the selection requirements is small but nonzero.

We consider a set of B_c^+ decay modes taken from the theoretical predictions of Kiselev [5]. Table XI shows the list of the B_c^+ decay modes and their branching fractions

TABLE IX. Total background for $B_c^+ \to J/\psi\mu^+X$ decays in three invariant-mass ranges. The doubly misidentified contribution is subtracted from the total to avoid double counting. Entries with no statistical uncertainties listed represent determinations for which the statistical uncertainty is negligible compared with the systematic uncertainty. Entries with no systematic uncertainties are estimated to have negligible systematic uncertainties compared with the statistical errors.

$B_c^+ \to J/\psi\mu^+X$ background	3–4 GeV/c^2	4–6 GeV/c^2	>6 GeV/c^2
Misidentified J/ψ	$11.5 \pm 2.4(\text{stat})$	$96.5 \pm 6.9(\text{stat})$	$25.0 \pm 3.5(\text{stat})$
Misidentified muon	$86.7^{+2.4}_{-4.2}(\text{syst})$	$344.4^{+9.6}_{-16.5}(\text{syst})$	$32.1^{+0.9}_{-1.5}(\text{syst})$
Doubly misidentified	$5.1^{+0.1}_{-0.2}(\text{syst})$	$19.0^{+0.5}_{-0.9}(\text{syst})$	$5.2^{+0.1}_{-0.3}(\text{syst})$
$b\bar{b}$ background	$12.4 \pm 2.4(\text{stat}) \pm 0.4(\text{syst})$	$178.6 \pm 12.4(\text{stat}) \pm 5.8(\text{syst})$	$110.4 \pm 10.7(\text{stat}) \pm 3.6(\text{syst})$
Total misidentified+$b\bar{b}$ bg.	$105.5 \pm 3.4(\text{stat})\ ^{+2.4}_{-4.2}(\text{syst})$	$600.5 \pm 14.2(\text{stat})\ ^{+11.2}_{-17.5}(\text{syst})$	$162.3 \pm 11.3(\text{stat})\ ^{+3.7}_{-3.9}(\text{syst})$

TABLE X. $B_c^+ \to J/\psi\mu^+X$ candidates and background subtractions from Table IX.

	3–4 GeV/c^2	4–6 GeV/c^2	>6 GeV/c^2
$N(B_c^+ \to J/\psi\mu^+X)$	132 ± 11.5	1370 ± 37.0	208 ± 14.4
Sum of misidentified + $b\bar{b}$ bg.	$105.5^{+4.2}_{-5.4}$	$600.5^{+18.1}_{-22.5}$	$162.3^{+11.9}_{-12.0}$
N_{obs}	$26.5^{+12.2}_{-12.7}$	$769.5^{+41.2}_{-43.3}$	45.7 ± 18.7

TABLE XI. B_c^+ decay modes and their BF_1 from the theoretical predictions of Kiselev [5]. The BF_2 column represents other decays and associated branching fractions necessary to reach the trimuon system. The "product BF Kiselev" represents the product $BF_1 BF_2$ for the Kiselev predictions [5], and the sum is normalized to 1. The "Ivanov" column represents a similar sum based on the theoretical predictions of Ivanov [6].

				Product BF	
B_c^+ decay mode	BF_1 pred	Secondary decay mode	BF_2	Kiselev	Ivanov
$J/\psi\mu^+\nu$	0.01900	None		0.8424	0.8872
$\psi(2S)\mu^+\nu$	0.00094	$\psi(2S) \to J/\psi + \cdots$	0.595	0.0248	0.0017
$B_s^0\mu^+\nu$	0.04030	$B_s^0 \to J/\psi + \cdots$	0.0137	0.0245	0.0065
$B_s^{*0}\mu^+\nu$	0.05060	$B_s^{*0} \to J/\psi + \cdots$	0.0137	0.0307	0.0139
$B^0\mu^+\nu$	0.00340	$B^0 \to J/\psi + \cdots$.	0.0109	0.0016	0.0003
$B^{*0}\mu^+\nu$	0.00580	$B^{*0} \to J/\psi + \cdots$	0.0109	0.0028	0.0003
$J/\psi\tau\nu$	0.00480	$\tau \to \mu + \cdots$	0.178	0.0378	0.0373
$\psi(2S)\tau\nu$	0.00008	$\psi(2S) \to J/\psi + \cdots$			
		$\tau \to \mu + \cdots$	0.595*0.178	0.0004	0.0000
$J/\psi D_s^+$	0.00170	$D_s^+ \to \mu + \cdots$	0.0864	0.0065	0.0126
$J/\psi D_s^{*+}$	0.00670	$D_s^{*+} \to \mu + \cdots$	0.0864	0.0257	0.0359
$J/\psi D^+$	0.00009	$D^+ \to \mu + \cdots$	0.168	0.0007	0.0011
$J/\psi D^{*+}$	0.00028	$D^{*+} \to \mu + \cdots$	0.168	0.0021	0.0032

used in the MC simulation. Another set of theoretical B_c^+ decay modes that is sufficiently complete to allow an estimate of the number of events in our signal sample from other B_c^+ decay modes is given by Ivanov and collaborators [6]. The difference in the estimate of the mumber of events from other decays modes from these two bodies of work is used to estimate the systematic uncertainty in this correction. The correction is small, approximately 30 events, but the two sets of branching-fraction predictions differ by approximately 50% of the correction. Using BGENERATOR [10], we generate $B_c^+ \to J/\psi\mu^+\nu$ decays and eleven other decay modes that can yield trimuon events. The fraction of these events that meets the selection requirements is reported in Table XII.

TABLE XII. Trimuon survival fractions for the various decay modes using the product of branching fractions based on the predictions of Kiselev B(K) [5]. The event fractions for each decay are determined from the MC simulation with the number of surviving events shown at the bottom of each column. The fractions in each column add to 1.0.

B_c^+ decay mode	B(K)	3–4 GeV/c^2	4–6 GeV/c^2	>6 GeV/c^2
$J/\psi\mu^+\nu$	0.8424	0.9007	0.9612	1.0
$\psi(2S)\mu^+\nu$	0.0248	0.0251	0.0200	0
$B_s^0\mu^+\nu$	0.0245	0.0114	0.0001	0
$B_s^{*0}\mu^+\nu$	0.0307	0.0160	0	0
$B^0\mu^+\nu$	0.0016	0	0	0
$B^{*0}\mu^+\nu$	0.0028	0.0011	0	0
$J/\psi\tau^+\nu$	0.0378	0.0411	0.0110	0
$\psi(2S)\tau^+\nu$	0.0004	0.0011	0.0001	0
$J/\psi D_s^+$	0.0065	0	0.0017	0
$J/\psi D_s^{*+}$	0.0257	0.0034	0.0056	0
$J/\psi D^+$	0.0007	0	0.0001	0
$J/\psi D^{*+}$	0.0021	0	0.0003	0
Total 3μ events		876	28342	1301

Our method uses the number $N_{\rm obs}$ of observed B_c^+ candidates in the data as shown in Table X after all other backgrounds have been subtracted except for the other decay modes. In the signal region 4–6 GeV/c^2, we observe $N_{\rm obs} = 769.5$ events. The number of $B_c^+ \to J/\psi\mu^+\nu$ events in the data is given by $N_{B_c^+} = N_{\rm obs} - N_{\rm other}$ where $N_{\rm other}$ is the number due to other decay modes. This can be rewritten as

$$N_{\rm other} = N_{\rm obs}\left(1 - \frac{N_{B_c^+}}{N_{\rm obs}}\right).$$

The fraction $N_{B_c^+}/N_{\rm obs}$ equals 0.961 for the signal region 4–6 GeV/c^2 and is given in Table XII. Thus, $N_{\rm other}$ is 30.0 ± 1.6(stat) events in the signal region and 2.6 ± 1.2(stat) events in the 3–4 GeV/c^2 mass range. The difference between the Kiselev and Ivanov predictions for the $B_c^+ \to J/\psi\mu^+\nu$ branching fraction is 9% [5,6]. This results in a systematic uncertainty of ± 16.3 events in $N_{B_c^+}$.

VI. B_c^+ SIGNAL

The estimated number of events from other decay modes that contribute to the $B_c^+ \to J/\psi\mu^+X$ signal and sidebands, observed $N_{\rm obs}$ and the final number $N_{B_c^+}$ of $B_c^+ \to J/\psi\mu^+\nu$, are shown in Table XIII. The statistical and systematic uncertainties are combined. The result for $N_{B_c^+}$ in the 3–4 GeV/c^2 and greater than 6 GeV/c^2 mass regions compared with the number of simulated $B_c^+ \to J/\psi\mu^+\nu$ events in these regions yields an important cross-check on the overall size of the experimental backgrounds in the 4–6 GeV/c^2 signal region. The 3–4 GeV/c^2 and greater than 6 GeV/c^2 mass regions are populated predominantly by background, while the signal region has

TABLE XIII. Final numbers of $B_c^+ \to J/\psi\mu^+\nu$, $N_{B_c^+}$. The statistical and systematic errors are combined. The last row presents the number of simulated $B_c^+ \to J/\psi\mu^+\nu$ events in the three mass regions. They are scaled so that the number in the signal region is consistent with the experimental data. The MC sample's statistical uncertainties are small compared with the statistical uncertainties in the experimental data.

Mass range (GeV/c^2)	3–4 GeV/c^2	4–6 GeV/c^2	>6 GeV/c^2
$N_{\rm obs}$	$26.5^{+12.2}_{-12.7}$	$769.5^{+41.2}_{-43.3}$	45.7 ± 18.7
Other decay modes	2.6 ± 1.9	30.0 ± 16.4	0
$N_{B_c^+}$	$23.9^{+12.3}_{-12.8}$	$739.5^{+44.3}_{-46.3}$	45.7 ± 18.7
$N(B_c^+ \to J/\psi\mu^+\nu)$, MC	22.8 ± 0.6	739.5	27.6 ± 0.6

740 $B_c^+ \to J/\psi\mu^+\nu$ decays and 630 background events including the other decay modes. By normalizing a Monte Carlo sample of $B_c^+ \to J/\psi\mu^+\nu$ events to the measured number of events after background subtraction in the signal region, we predict the expected number of $B_c^+ \to J/\psi\mu^+\nu$ decays in the 3–4 GeV/c^2 and greater than 6 GeV/c^2 mass regions. From Table XIII, we expect 23 $B_c^+ \to J/\psi\mu^+\nu$ decays and observe 24 ± 12 in the 3–4 GeV/c^2 mass region. In the greater than 6 GeV/c^2 region, we expect 28 and observe 46 ± 19. This gives confidence in the calculation of the sum of background yield plus other decay modes in the signal region.

The invariant-mass distribution of the $J/\psi\mu^+$ events is shown in Fig. 21 with simulated signal and backgrounds superimposed. "Misid. muon" is the misidentified-muon background corrected for the doubly misidentified background, while "other modes" indicates the contribution from the other decay modes. "B_c Monte Carlo" stands for simulated $B_c^+ \to J/\psi\mu^+\nu$ decays. The simulated sample size is normalized to the number of signal events in the signal region after subtracting background and other decay modes. After accounting for the small $B_c^+ \to J/\psi\mu^+\nu$ signal component in the 3–4 GeV/c^2 and greater than 6 GeV/c^2 mass regions, we correctly model the background in these regions.

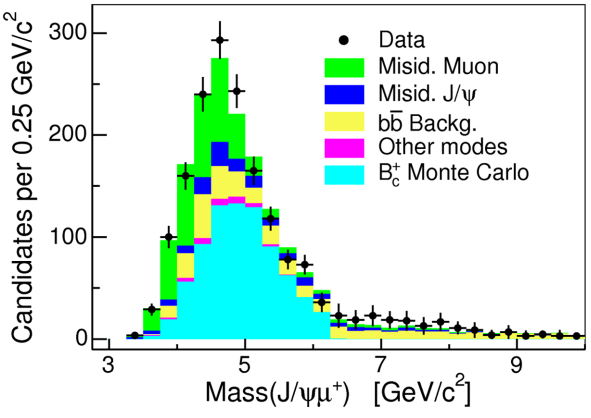

FIG. 21. Invariant-mass distribution of the $B_c^+ \to J/\psi\mu^+$ candidate events using the full CDF Run II data sample with a MC simulated signal sample and the calculated backgrounds superimposed. Details of the contributions are described in the main text. The error bars are the statistical uncertainties on the data and background predictions combined.

VII. RELATIVE EFFICIENCY OF $B^+ \to J/\psi K^+$ TO $B_c^+ \to J/\psi\mu^+\nu$

To determine $\mathcal{R}$, we need to determine the efficiencies used in Eq. (2). These efficiencies are collected together into $\epsilon_{\rm rel} = \epsilon_{B^+}/(\epsilon_{B_c^+} \times \epsilon_\mu)$. The efficiencies ϵ_{B^+} and $\epsilon_{B_c^+}$ are the geometrical acceptances for $B^+ \to J/\psi K^+$ and $B_c^+ \to J/\psi\mu^+\nu$ decays, respectively, in the CDF II detector corrected for effects discussed below, and ϵ_μ is the third-muon detection efficiency in the CMU and CMP detectors. The ratio $\epsilon_{B^+}/\epsilon_{B_c^+}$ includes a small correction for the relative trigger efficiency between kaons and muons. The muon identification efficiency for CMUP muons is $0.962 \pm 0.007({\rm stat}) \pm 0.021({\rm syst})$ [34]. Because the effects due to multiple Coulomb scattering and the stopping of muons in the absorber at low p_T are modeled accurately by the simulation, the normalized efficiency of the CMUP is uniform over the p_T range greater than 3 GeV/c.

We determine the efficiencies ϵ_{B^+} and $\epsilon_{B_c^+}$ with MC simulations. Knowledge of the transverse momentum spectra for the B^+ and B_c^+ is essential to determine the relative efficiency correctly. In order to determine the relative efficiency, we use the generated samples of $B^+ \to J/\psi K^+$, $B_c^+ \to J/\psi\mu^+\nu$, and $B_c^{*+} \to B_c^+ + \gamma$ decays. All data from the MC events are passed through the full detector and trigger simulation. The events that meet the dimuon trigger requirements are processed in the same way as experimental data.

A. B^+ and B_c^+ p_T spectra

The $B^+ \to J/\psi K^+$ acceptance calculation is based on the FONLL spectrum [3], where FONLL stands for fixed-order plus next-to-leading logs. As the FONLL spectrum shows some discrepancies in the low-p_T region with respect to the data, a corrected FONLL spectrum is used.

In generating the $B_c^+ \to J/\psi\mu^+\nu$ MC sample, we follow the theoretical work on B_c^+ production, the general-mass variable-flavor-number (GMVFN) model of Chang *et al.* [35], which has the following advantages: it includes B_c^+ and B_c^{*+} spectra; it includes production via the interactions of gluons and heavy sea quarks, gb and gc, as well as pure gg fusion; and it includes a small contribution from $q\bar{q}$ production. Figure 22 shows that the B_c^+ and B_c^{*+} spectra are similar, but the B_c^+ produced in $B_c^{*+} \to B_c^+\gamma$ decays is

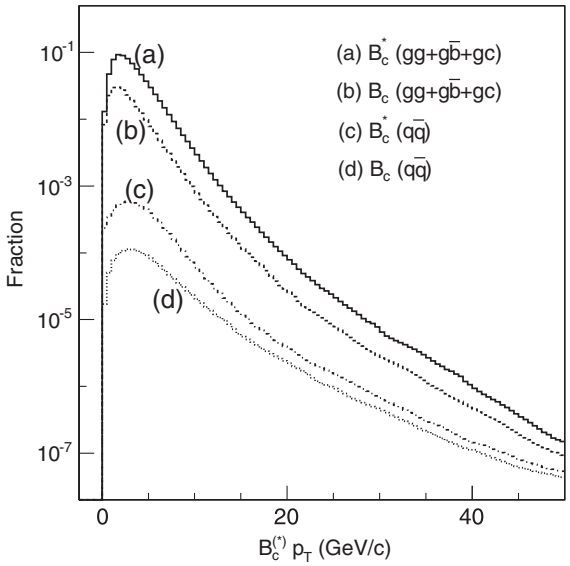

FIG. 22. Spectra for B_c^+ and B_c^{*+} due to various production processes are shown. The processes are scaled to reflect the weight used in composing the final spectrum.

softer than that produced directly. The composition of the B_c^+ spectrum used in this measurement makes use of the B_c^+ and B_c^{*+} cross sections given in Tables I–II of Ref. [35]. According to this calculation, made for Tevatron energy 1.96 TeV using $p_T(B_c^+) > 4$ GeV/c and rapidity $|y| < 0.6$, the total production cross sections for the B_c^+ and B_c^{*+} mesons are 0.7 and 2.3 nb, respectively. In Table XIV we present both the combined contributions of $gg + g\bar{b} + gc$ and $q\bar{q}$ to B_c^+ and B_c^{*+} production.

The authors of Ref. [35] provided the p_T and rapidity distributions for both B_c^+ and B_c^{*+} mesons from the various production mechanisms.

In the MC simulation, we assign the B_c^{*+} mass to be $M_{B_c^+} + 0.076$ GeV/c^2 based on the theoretically predicted value from Baldicchi and Prosperi [7]. In this work the authors predict a range of B_c^{*+} masses varying with the model used. We use the highest of the predicted B_c^{*+} masses in order to assign a conservative systematic uncertainty on the amount of B_c^{*+} production relative to B_c^+ production. The mass difference between the B_c^{*+} and the B_c^+ is too small for π^0 production. Consequently, the B_c^{*+} are assumed to decay exclusively to the $B_c^+\gamma$ final state.

TABLE XIV. Cross section fractions for B_c^+ and B_c^{*+} based on calculations from Ref. [35], where "$gg + g\bar{b} + gc$" represents the combined contributions from the gg fusion, $g\bar{b}$ and gc production subprocesses, and $q\bar{q}$ represents the quark-antiquark production mechanism.

Production fractions	$gg + g\bar{b} + gc$	$q\bar{q}$
B_c^+	0.994	0.006
B_c^{*+}	0.991	0.009

B. Comparison of MC B^+ and B_c^+ p_T spectra with data

The $B_c^+ \to J/\psi\mu^+\nu$ and $B^+ \to J/\psi K^+$ samples generated using the corrected p_T spectra are compared with data in Fig. 23, where the same selection requirements are applied to data and simulation. Experimental data and simulated distributions are selected with the requirement that the invariant-mass value should lie within the signal mass region 4–6 GeV/c^2 for the B_c^+ and within ± 50 MeV/c^2 of the B^+ mass for the $B^+ \to J/\psi K^+$ decays. Both p_T distributions for data are background subtracted. The simulated distributions are normalized to the data distributions.

C. Results for the relative efficiency

In calculating $\epsilon_{\rm rel}$, we first determine $\epsilon_{B_c^+}$ and ϵ_{B^+} separately and then calculate the ratio $\epsilon_{\rm rel} = \epsilon_{B^+}/(\epsilon_{B_c^+} \times \epsilon_\mu)$ for $p_T(B) > 6$ GeV/c, where B is the B_c^+ (B^+) for the $\epsilon_{B_c^+}$ (ϵ_{B^+}) calculations. For $\epsilon_{B_c^+}$ and ϵ_{B^+}, both the generated and reconstructed events are determined from a sample with a generator-level requirement of $p_T(B) > 6$ GeV/c. The generator-level B_c^+ or B^+ events that satisfy $p_T(B) > 6$ GeV/c and $|y| < 1.0$ are counted in this sample as the

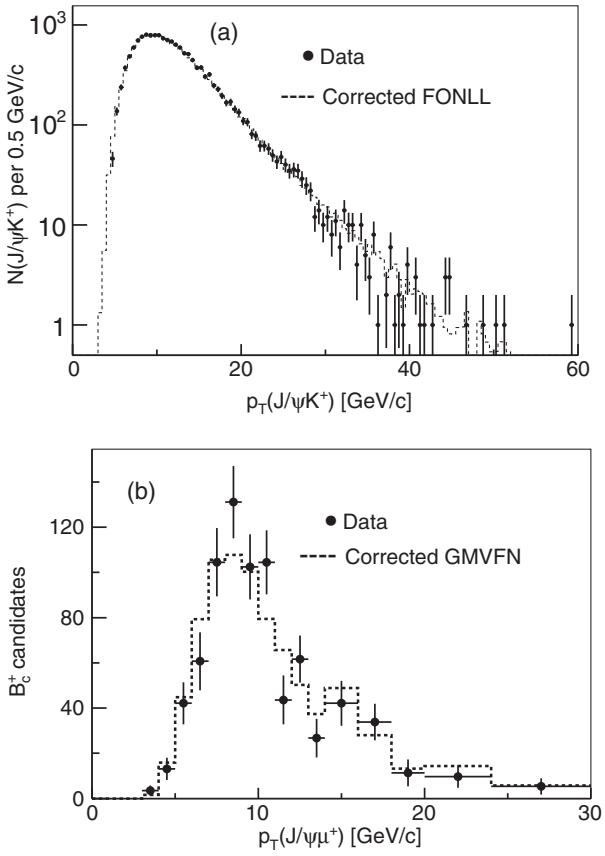

FIG. 23. Transverse momenta distributions for (a) the $J/\psi K^+$ and (b) the $J/\psi\mu^+$ samples. Both data plots are background subtracted, and the theoretically predicted spectra are corrected using data.

TABLE XV. B_c^+ acceptance for different production mechanisms.

	$gg + g\bar{b} + gc$		$q + \bar{q}$	
Production process	B_c^+	$B_c^{*+} \to B_c^+\gamma$	B_c^+	$B_c^{*+} \to B_c^+\gamma$
$\epsilon_{B_c^+}$ (%)	0.179 ± 0.001	0.172 ± 0.001	0.342 ± 0.001	0.252 ± 0.001

generated events, while all events are passed through the detector and trigger simulation with all the analysis selection criteria applied. Finally, a requirement that the p_T be greater than 6 GeV/c is applied to the reconstructed $J/\psi\mu^+$ in the B_c^+ case and to the reconstructed $J/\psi K^+$ in the B^+ case. For the reconstructed events there is no requirement made on the rapidity. In both cases $\epsilon_{B_c^+(B^+)}$ is the ratio of reconstructed to generated events.

In the acceptance calculation there is a small correction (approximately 3.4% in the value of $\epsilon_{\rm rel}$) for the fact that XFT efficiencies in data are different for kaons and muons. Assuming that muons and pions are similar, the model, based on data, parametrizes the XFT efficiency for kaons and pions as a function of $1/p_T$ relative to the same efficiencies as estimated in the MC simulation for the acceptance [36]. The muon efficiency ϵ_μ depends on the CMU and CMP muon detectors alone and is not included in these results.

The results for the acceptances of $B_c^+ \to J/\psi\mu^+\nu$ decays for the various B_c^+ production mechanisms as discussed in Sec. VII A are shown in Table XV. Using the production cross-section fractions for B_c^+ and B_c^{*+} given in Table XIV combined with the predicted production cross sections for B_c^+ and B_c^{*+} of 0.7 and 2.3 nb, respectively, a weighted average of the acceptances is calculated to determine the total acceptance $\epsilon_{B_c^+}$ for $B_c^+ \to J/\psi\mu^+\nu$ presented in Table XVI. The acceptance ϵ_{B^+} for $B^+ \to J/\psi K^+$ is also shown in Table XVI and its calculation is simpler because there is only one production spectrum involved in its determination. Both results are for $p_T(B) > 6$ GeV/c. Comparisons of the acceptances for the $J/\psi\mu^+$ and $J/\psi K^+$ systems and the $\epsilon_{B^+}/\epsilon_{B_c^+}$ ratio as a function of the rapidity are shown in Fig. 24. Using ϵ_{B^+} and $\epsilon_{B_c^+}$ from Table XVI and ϵ_μ from the opening of Sec. VII, the value of $\epsilon_{\rm rel}$ is

$$\epsilon_{\rm rel} = 4.093 \pm 0.038({\rm stat}). \tag{11}$$

Using Eq. (2), $N_{B_c^+}$ from Table XIII, N_{B^+} from Fig. 4(b), and $\epsilon_{\rm rel}$, we find

$$\mathcal{R} = 0.211 \pm 0.012({\rm stat}). \tag{12}$$

TABLE XVI. Acceptances of B_c^+ and B^+ for $p_T > 6$ GeV/c. Small corrections for different XFT track efficiencies for muons and kaons are applied.

	$B^+ \to J/\psi K^+$	$B_c^+ \to J/\psi\mu^+\nu$
ϵ_{B^+,B_c^+} (%)	0.688 ± 0.002	0.175 ± 0.001

D. Systematic uncertainties for the relative efficiency

We consider the systematic uncertainty associated with the prediction of the relative efficiency due to knowledge of the B_c^+ lifetime, the B_c^+ production spectrum, the B^+ production spectrum, the difference between the K and μ tracking efficiencies in the XFT, and the muon identification efficiency for CMUP muons. The total systematic uncertainty in $\epsilon_{\rm rel}$ is summarized in Table XVII. The individual systematic uncertainties are discussed below.

1. Systematic uncertainty from the B_c^+ lifetime

The systematic uncertainty for $\epsilon_{\rm rel}$ due to the uncertainty in the B_c^+ lifetime is estimated by varying the B_c^+ lifetime in MC simulations by one standard deviation relative to the current world average value [4]. The systematic uncertainty is $\Delta\epsilon_{\rm rel} = {}^{+0.134}_{-0.147}$.

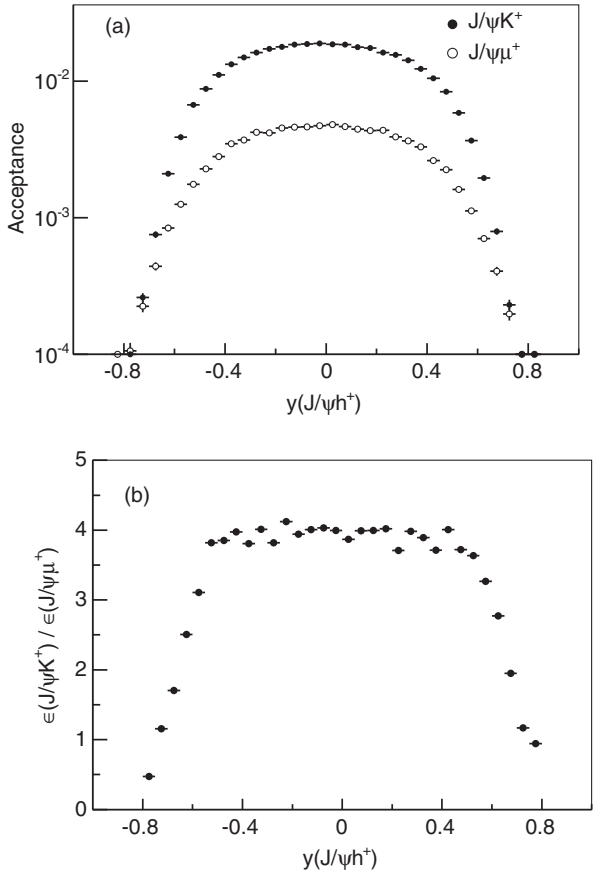

FIG. 24. (a) Comparison of the acceptances for the $J/\psi\mu^+$ and $J/\psi K^+$ systems and (b) the $\epsilon_{B^+}/\epsilon_{B_c^+}$ ratio as a function of the rapidity.

TABLE XVII. Systematic uncertainty assigned to $\epsilon_{\rm rel}$.

Source	Systematic uncertainty
B_c^+ lifetime	$^{+0.134}_{-0.147}$
B_c^+ spectrum	$^{+0.356}_{-0.303}$
B^+ spectrum	± 0.055
XFT efficiency	± 0.070
CMUP muon efficiency	$^{+0.092}_{-0.087}$
Total	$^{+0.401}_{-0.359}$

2. Systematic uncertainty from the B_c^+ and B^+ production spectra

The systematic uncertainty associated with the calculations of the B_c^+ and B^+ production spectra is derived by comparing the bin-by-bin p_T spectrum given by the data directly with that of simulated events produced using the corrected theoretical production spectra (see Fig. 23). The ratios of the data to the MC simulation versus $p_T(J/\psi K^+)$ for the B^+ mesons and versus $p_T(J/\psi\mu^+)$ for the B_c^+ mesons are shown in Fig. 25.

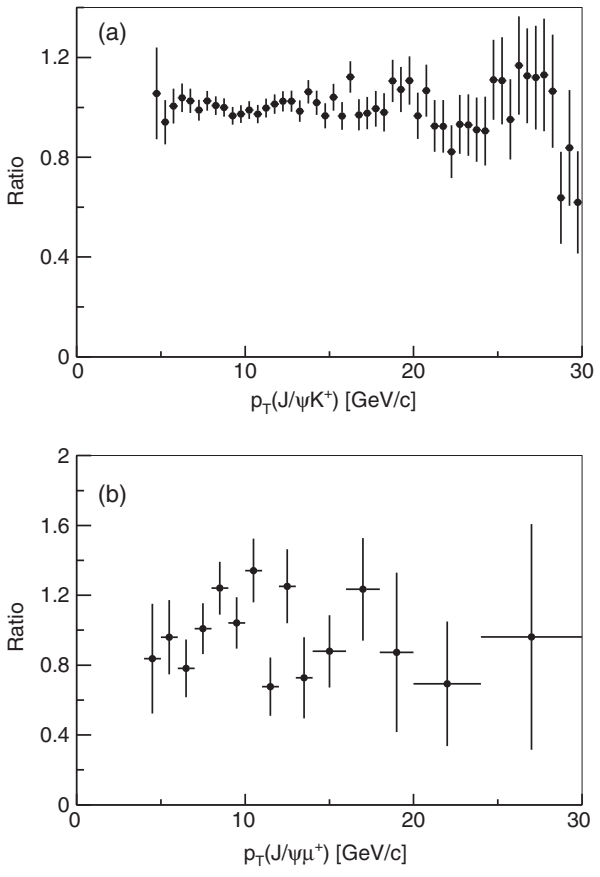

FIG. 25. Ratio of the data to the MC simulation (a) versus $p_T(J/\psi K^+)$ for the B^+ and (b) versus $p_T(J/\psi\mu^+)$ for the B_c^+. Both theoretically predicted spectra are corrected using data.

The data to corrected-MC ratio plots (Fig. 25) for both cases are used to estimate an average ratio for $p_T(B) > 6$ GeV/c, $\bar{R} = \sum(w_i \times R_i)/\sum w_i$, where i is the bin number, R_i is the ratio in bin i, $w_i = 1/\sigma_i^2$ and $\sigma_{\bar{R}} = \sqrt{\sum \sigma_i^2/[n(n-1)]}$. Thus, we find $\bar{R}(B_c^+) = 1.00 \pm 0.08$ and $\bar{R}(B^+) = 0.999 \pm 0.013$. We assign systematic uncertainties of 8% and 1.3% for the B_c^+ and B^+ ratios, respectively. The $\epsilon_{\rm rel}$ systematic uncertainties are $^{+0.356}_{-0.303}$ for the B_c^+ and ± 0.055 for the B^+ spectra, respectively.

3. Differences in the efficiency of kaons and muons in the XFT simulation

A small source of systematic uncertainty arises from the different XFT efficiencies for kaons and muons due to the different dE/dx characteristics of these particles in the COT. The difference in ionization gives different single-hit efficiencies for kaons and muons that result in different XFT efficiencies as functions of p_T. These differences are not modeled in the simulations. We model this systematic uncertainty by weighting the MC simulation to reproduce kaon and pion transverse-momentum distributions with and without the XFT efficiencies determined from data [36]. The $\epsilon_{\rm rel}$ difference between using and not using the XFT correction is 0.14. Comparison of the MC simulation with experimental data gives a systematic uncertainty of 50% of the correction or ± 0.07.

4. Muon identification efficiency

We use Ref. [34] for the muon identification efficiency for CMUP muons and its systematic uncertainty to calculate the contribution to the uncertainty in $\epsilon_{\rm rel}$. The measured systematic uncertainty for the detection efficiency of CMUP muons is about 2.2%. It yields a systematic uncertainty for $\epsilon_{\rm rel}$ of $\Delta\epsilon_{\rm rel} = ^{+0.092}_{-0.087}$.

TABLE XVIII. Summary of values and uncertainties used in the measurement of $\mathcal{R}$ for $p_T > 6$ GeV/c and $|y| < 0.6$.

Quantity	Value
$N(B_c^+ \to J/\psi\mu^+\nu)$	$740 \pm 45(\text{stat} + \text{syst})$
$N(B^+ \to J/\psi K^+)$	$14338 \pm 125(\text{stat})$
$\epsilon_{\rm rel}$	$4.09 \pm 0.04(\text{stat})^{+0.40}_{-0.36}(\text{syst})$
$\mathcal{R}$	$0.211 \pm 0.012(\text{stat})^{+0.021}_{-0.020}(\text{syst})$

TABLE XIX. Systematic uncertainties for $\mathcal{R}$.

Source	Systematic uncertainty
B_c^+ background	$^{+0.0057}_{-0.0068}$
$\epsilon_{\rm rel}$	$^{+0.0207}_{-0.0185}$
Total	$^{+0.0214}_{-0.0197}$

TABLE XX. Branching-fraction predictions for the decay $B_c^+ \to J/\psi\mu^+\nu$.

	Branching-fraction predictions in %												
Reference	[5]	[39]	[40]	[41]	[6]	[42]	[43]	[44]	[45]	[46]	[47]	[48]	[49]
Prediction	1.9	2.37	1.44	1.21	2.07	2.35	1.5	1.2	1.49	1.15	1.47	2.01	6.7

VIII. RESULTS AND CONCLUSIONS

The result of the measurement of $\mathcal{R}$ based on the complete CDF Run II data set, which corresponds to an integrated luminosity of 8.7 fb^{-1} is

$$\mathcal{R} = 0.211 \pm 0.012(\text{stat}) \, {}^{+0.021}_{-0.020} \, (\text{syst}) \qquad (13)$$

for $p_T(B_c^+) > 6$ GeV/c and $|y| < 0.6$. The numbers of $B_c^+ \to J/\psi\mu^+\nu$ and $B^+ \to J/\psi K^+$ decays, and the relative efficiency between the two, are summarized in Table XVIII. The total systematic uncertainties for the ratio $\mathcal{R}$ are summarized in Table XIX.

The result $\mathcal{R} = 0.211 \pm 0.024$ can be compared to the Run I measurement from CDF [37], $\mathcal{R} = 0.13 \pm 0.06$ based on a sample corresponding to 0.11 fb^{-1} of integrated luminosity at $\sqrt{s} = 1.8$ TeV.

Using theoretical predictions for $\mathcal{B}(B_c^+ \to J/\psi\mu^+\nu)$ and independent measurements for $\mathcal{B}(B^+ \to J/\psi K^+)$ and $\sigma(B^+)$, we calculate the total B_c^+ cross se ction. The measured quantities are $\mathcal{B}(B^+ \to J/\psi K^+) = (1.027 \pm 0.031) \times 10^{-3}$ [4] and $\sigma(B^+) = 2.78 \pm 0.24$ μb for $p_T(B^+) > 6$ GeV/c and $|y| < 1$ [38]. Assuming that the observed value of $\mathcal{R}$ for $|y| < 0.6$ approximates the value for $|y| < 1$, we find

$$\sigma(B_c^+)\mathcal{B}(B_c^+ \to J/\psi\mu^+\nu) = 0.602 \pm 0.034(\text{stat}) \, {}^{+0.060}_{-0.063} \, (\text{syst}) \pm 0.055(\text{other}) \text{ nb} \qquad (14)$$

for $p_T(B_c^+) > 6$ GeV/c and $|y| < 1$. In Eq. (14) the statistical and systematic uncertainties are from the measurement of $\mathcal{R}$ and other is the combined experimental uncertainty in the measurements of $\mathcal{B}(B^+ \to J/\psi K^+)$ and $\sigma(B^+)$. Combining the uncertainties in quadrature gives $\sigma(B_c^+)\mathcal{B}(B_c^+ \to J/\psi\mu^+\nu) = 0.60 \pm 0.09$ nb. To extract the total B_c^+ production cross section from this result, it is necessary to consider the predictions for the branching fraction for the semileptonic decay $B_c^+ \to J/\psi\mu^+\nu$. Table XX summarizes the many predictions. The approaches to the calculation of this semileptonic branching fraction include QCD sum rules [5,39], relativistic constituent-quark models [6,40,41], a quark model using the Bethe-Salpeter equation [42], a nonrelativistic constituent-quark model [43], covariant-light-front quark models [44–46], QCD relativistic-potential models [47,48], and nonrelativistic QCD [49]. With the exception of Ref. [49], all of the theoretical results shown in Table XX predict the branching fraction $\mathcal{B}(B_c^+ \to J/\psi\mu^+\nu)$ in the range 1.15%–2.37%. Using this selection of theoretical predictions, we find the total B_c^+ cross section to be in the range 25 ± 4 to 52 ± 8 nb for $p_T(B_c^+) > 6$ GeV/c and $|y| < 1$, where the uncertainties reflect only the experimental uncertainties of the measurements used in the calculation. The result is a measure of the combined cross section for production to the ground state plus any excited B_c^+ state that cascades into the ground state prior to its weak-interaction decay.

This result is higher than the theoretical prediction of Chang *et al.*, [2,35], which estimates the sum of the production cross sections to B_c^+ and B_c^{*+}, $\sigma(B_c^+ + B_c^{*+})$, to be 5 nb for $\sqrt{s} = 1.96$ TeV, $p_T > 4$ GeV/c, and $|y| < 1$. Similarly, Ref. [50] reports $\sigma(B_c^+ + B_c^{*+}) = 7.4 \pm 5.4$ nb for $\sqrt{s} = 1.8$ TeV, $p_T > 6$ GeV/c, and $|y| < 1$. If we consider the prediction $\mathcal{B}(B_c^+ \to J/\psi\mu^+\nu) = 6.7^{+2.5}_{-1.4}\%$ given in Ref. [49], then our result for the B_c^+ production cross section is $9.0^{+3.6}_{-2.3}$ nb (theoretical uncertainty included), in reasonable agreement with the predictions of Refs. [2,35,50].

If the branching fraction $\mathcal{B}(B_c^+ \to J/\psi\mu^+\nu)$ is in the approximate range 1.2%–2.4% as given by 12 of the 13 predictions in Table XX, then there is a discrepancy between the theoretical B_c^+ production cross section and the estimate made from the experimental results presented here. This discrepancy would be mitigated if the production cross section to B_c^+ states higher in mass than the B_c^{*+} were also large. Therefore, it would be very useful to have a new prediction of the B_c^+ production cross section at the exact kinematic values of this experimental result that takes into account all production to excited B_c^+ states that cascade to the ground state. The discrepancy would also disappear if $\mathcal{B}(B_c^+ \to J/\psi\mu^+\nu)$ is approximately 7% as predicted by Ref. [49].

ACKNOWLEDGMENTS

We thank the Fermilab staff and the technical staffs of the participating institutions for their vital contributions. This work was supported by the U.S. Department of Energy and National Science Foundation; the Italian Istituto Nazionale di Fisica Nucleare; the Ministry of Education, Culture, Sports, Science and Technology of Japan; the Natural Sciences and Engineering Research Council of Canada; the National Science Council of the Republic of China; the Swiss National Science Foundation; the A. P. Sloan

Foundation; the Bundesministerium für Bildung und Forschung, Germany; the Korean World Class University Program, the National Research Foundation of Korea; the Science and Technology Facilities Council and the Royal Society, United Kingdom; the Russian Foundation for Basic Research; the Ministerio de Ciencia e Innovación, and Programa Consolider-Ingenio 2010, Spain; the Slovak R&D Agency; the Academy of Finland; the Australian Research Council (ARC); and the EU community Marie Curie Fellowship Contract No. 302103.

[1] Charge-conjugate states are implied throughout the paper unless otherwise specified.
[2] C.-H. Chang, C.-F. Qiao, J.-X. Wang, and X.-G. Wu, Phys. Rev. D **71**, 074012 (2005).
[3] M. Cacciari, S. Frixione, M. L. Mangano, P. Nason, and G. Ridolfi, J. High Energy Phys. 07 (2004) 033.
[4] K. A. Olive (Particle Data Group), Chin. Phys. C **38**, 090001 (2014).
[5] V. V. Kiselev, arXiv:hep-ph/0308214.
[6] M. A. Ivanov, J. G. Korner, and P. Santorelli, Phys. Rev. D **73**, 054024 (2006).
[7] M. Baldicchi and G. M. Prosperi, Phys. Rev. D **62**, 114024 (2000).
[8] C.-H. Chang, J.-X. Wang, and X.-G. Wu, Phys. Rev. D **70**, 114019 (2004).
[9] T. Aaltonen *et al.* (CDF Collaboration), Nucl. Instrum. Methods Phys. Res., Sect. A **526**, 249 (2004).
[10] D. Acosta *et al.* (CDF Collaboration), Phys. Rev. D **71**, 032001 (2005).
[11] A. Sill, Nucl. Instrum. Methods Phys. Res., Sect. A **447**, 1 (2000).
[12] T. Aaltonen *et al.*, Nucl. Instrum. Methods Phys. Res., Sect. A **729**, 153 (2013).
[13] A. A. Affolder *et al.*, Nucl. Instrum. Methods Phys. Res., Sect. A **453**, 84 (2000).
[14] A. A. Affolder *et al.*, Nucl. Instrum. Methods Phys. Res., Sect. A **526**, 249 (2004).
[15] D. Tonelli, Ph.D. thesis, Scuola Normale Superiore di Pisa, 2006 [Report No. FERMILAB-THESIS-2006-23].
[16] D. Acosta *et al.*, Nucl. Instrum. Methods Phys. Res., Sect. A **518**, 605 (2004).
[17] S. Cabrera *et al.*, Nucl. Instrum. Methods Phys. Res., Sect. A **494**, 416 (2002).
[18] G. Ascoli, L. E. Holloway, I. Karliner, U. E. Kruse, R. D. Sard, V. J. Simaitis, D. A. Smith, and T. K. Westhusing, Nucl. Instrum. Methods Phys. Res., Sect. A **268**, 33 (1988).
[19] R. Blair *et al.* (CDF Collaboration), Report No. FERMILAB-PUB-96-390-E, 1996.
[20] E. J. Thomson *et al.*, IEEE Trans. Nucl. Sci. **49**, 1063 (2002).
[21] S. Holm, J. Freeman, R. Klein, J. D. Lewis, T. M. Shaw, and C. Ciobanu, IEEE Trans. Nucl. Sci. **47**, 895 (2000).
[22] K. Anikeev *et al.*, IEEE Trans. Nucl. Sci. **53**, 653 (2006).
[23] W. Ashmanskas *et al.*, Nucl. Instrum. Methods Phys. Res., Sect. A **518**, 532 (2004).
[24] Y. S. Chung *et al.*, IEEE Trans. Nucl. Sci. **52**, 1212 (2005).
[25] G. Giurgiu, Ph.D. thesis, Carnegie Mellon University, 2005 [Report No. FERMILAB-THESIS-2005-41].
[26] M. P. Hartz, Ph.D. thesis, University of Pittsburgh, 2008 [Report No. FERMILAB-THESIS-2008-82].
[27] R. Aaij *et al.* (LHCb Collaboration), Phys. Rev. D **85**, 091105(R) (2012).
[28] T. Sjöstrand, S. Mrenna, and P. Skands, J. High Energy Phys. 05 (2006) 026.
[29] H. L. Lai, J. Huston, S. Kuhlmann, J. Morfin, F. Olness, J. F. Owens, J. Pumplin, and W. K. Tung (CTEQ Collaboration), Eur. Phys. J. C **12**, 375 (2000).
[30] B. Andersson, G. Gustafson, G. Ingelman, and T. Sjöstrand, Phys. Rep. **97**, 31 (1983).
[31] B. Andersson, G. Gustafson, and B. Söderberg, Z. Phys. C **20**, 317 (1983).
[32] R. Brun *et al.*, GEANT3, Report No. CERN-DD-EE-84-1, 1987.
[33] R. D. Field, Phys. Rev. D **65**, 094006 (2002).
[34] A. Abulencia *et al.* (CDF Collaboration), J. Phys. G **34**, 2457 (2007).
[35] C.-H. Chang, C.-F. Qiao, J.-X. Wang, and X.-G. Wu, Phys. Rev. D **72**, 114009 (2005).
[36] K. R. Gibson, Ph.D. thesis, Carnegie Mellon University, 2006 [Report No. FERMILAB-THESIS-2006-09].
[37] F. Abe *et al.* (CDF Collaboration), Phys. Rev. Lett. **81**, 2432 (1998); Phys. Rev. D **58**, 112004 (1998).
[38] A. Abulencia *et al.* (CDF Collaboration), Phys. Rev. D **75**, 012010 (2007).
[39] Z.-H. T. Huang, X.-G. Li, Wu, and F. Zuo, Int. J. Mod. Phys. A **23**, 3237 (2008).
[40] M. A. Nobes and R. M. Woloshyn, J. Phys. G **26**, 1079 (2000).
[41] D. Ebert, R. N. Faustov, and V. O. Galkin, Phys. Rev. D **68**, 094020 (2003).
[42] C. H. Chang and Y. Q. Chen, Phys. Rev. D **49**, 3399 (1994).
[43] E. Hernandez, J. Nieves, and J. M. Verde-Velasco, Phys. Rev. D **74**, 074008 (2006).
[44] A. Y. Anisimov, I. M. Narodetsky, C. Semay, and B. Silvestre-Brac, Phys. Lett. B **452**, 129 (1999).
[45] W. Wang, Y. L. Shen, and C. D. Lü, Phys. Rev. D **79**, 054012 (2009).
[46] H.-W. Ke, T. Liu, and X.-Q. Li, Phys. Rev. D **89**, 017501 (2014).
[47] P. Colangelo and F. De Fazio, Phys. Rev. D **61**, 034012 (2000).
[48] A. Abd El-Hady, J. H. Muñoz, and J. P. Vary, Phys. Rev. D **62**, 014019 (2000).
[49] C. F. Qiao and R. L. Zhu, Phys. Rev. D **87**, 014009 (2013).
[50] V. A. Saleev and D. V. Vasin, Phys. Lett. B **605**, 311 (2005).